Journal of Industrial and Engineering Chemistry xxx (xxxx) xxx

Contents lists available at ScienceDirect

Journal of Industrial and Engineering Chemistry

journal homepage: www.elsevier.com/locate/jiec

Full Length Article

# Sustainable recovery of rare earth elements from aqueous media using fruit pomaces: adsorption performance, thermodynamics, and environmental assessment

Salvatore Giovanni Michele Raccuia [a], Emanuele Zanda [a], Clemente Bretti [a], Mauro Formica [b], Eleonora Macedi [b], Andrea Melchior [c], Marilena Tolazzi [c], Alberto Pettignano [d], Nicola Muratore [d], Davide Lascari [d], Edoardo Teresi [e], Cristian Chiavetta [f], Giovanna De Luca [a], Anna Irto [a], Concetta De Stefano [a], Paola Cardiano [a,*], Gabriele Lando [a]

[a] Dipartimento di Scienze Chimiche, Biologiche, Farmaceutiche e Ambientali, Università degli Studi di Messina 98166 Messina, Italy
[b] Dipartimento di Scienze Pure e Applicate, Università degli Studi di Urbino "Carlo Bo", 61029 Urbino, Italy
[c] Dipartimento Politecnico di Ingegneria e Architettura, Laboratorio di Tecnologie Chimiche, Università di Udine 33100 Udine, Italy
[d] Dipartimento di Fisica e Chimica– Emilio Segré, Università di Palermo I-90128 Palermo, Italy
[e] Dipartimento di Ingegneria Civile, Chimica, Ambientale e dei Materiali "DICAM", Università di Bologna 40121 Bologna, Italy
[f] Dipartimento Sostenibilità (SSPT), ENEA, 00123 Roma, Italy

ARTICLE INFO

*Keywords:*
Critical raw material
Adsorption
Kinetics
Isothermal titration calorimetry
Sustainability
Life cycle assessment

ABSTRACT

The valorization of waste biomasses for recovering Critical Raw Materials (CRMs), particularly Rare Earth Elements (REEs), is a promising approach to enhance sustainability and resource efficiency. This study investigates the adsorption performance of bergamot, grape, and olive pomaces toward $Nd^{3+}$ and $Dy^{3+}$ ions under varying pH conditions, both in the absence of an ionic medium and in 0.10 mol/dm$^3$ $NaNO_3$(aq), following different biomass pretreatment protocols. Comparative tests with $La^{3+}$ enabled evaluation of light ($Nd^{3+}$, $La^{3+}$) *vs.* heavy ($Dy^{3+}$) lanthanide ion behavior. Biomass characterization was performed using Attenuated Total Reflectance Fourier Transform Infrared (ATR FT-IR) spectroscopy and Scanning Electron Microscopy – Energy-Dispersive X-ray (SEM-EDX) analysis to assess changes in surface chemistry and morphology after adsorption. Kinetic and isotherm analyses showed pseudo-second-order kinetics and Langmuir behavior, respectively. The highest capacity was observed for water-pretreated bergamot pomace at 30 °C, pH 5.0, without ionic medium, and measured adsorption efficiency followed the trend: $Dy^{3+}$ (0.45 mmol/g) > $Nd^{3+}$ (0.38 mmol/g) > $La^{3+}$ (0.35 mmol/g). The materials exhibited good reusability across adsorption/desorption cycles, supporting their potential as sustainable biosorbents. For the first time, direct isothermal titration calorimetry (ITC) was used to determine adsorption thermodynamics. Life Cycle Assessment (LCA) and Techno-Economic Assessment (TEA) further evaluated the environmental and economic feasibility of bergamot pomace under different processing scenarios.

## Introduction

In recent years, the search for sustainable resource management has grown driven by the depletion of conventional mineral resources and the increasing demand for high-tech applications based on CRMs (Critical Raw Materials), such as REEs (Rare Earth Elements) [1]. These elements

* Corresponding author.
*E-mail addresses:* saraccuia@unime.it (S.G.M. Raccuia), emanuele.zanda@unime.it (E. Zanda), cbretti@unime.it (C. Bretti), mauro.formica@uniurb.it (M. Formica), eleonora.macedi@uniurb.it (E. Macedi), andrea.melchior@uniud.it (A. Melchior), marilena.tolazzi@uniud.it (M. Tolazzi), alberto.pettignano@unipa.it (A. Pettignano), nicola.muratore@unipa.it (N. Muratore), davide.lascari@unipa.it (D. Lascari), edoardo.teresi@unibo.it (E. Teresi), cristian.chiavetta@enea.it (C. Chiavetta), delucag@unime.it (G. De Luca), airto@unime.it (A. Irto), cdestefano@unime.it (C. De Stefano), paola.cardiano@unime.it (P. Cardiano), glando@unime.it (G. Lando).

https://doi.org/10.1016/j.jiec.2025.09.008
Received 16 June 2025; Received in revised form 19 August 2025; Accepted 6 September 2025
Available online 8 September 2025


Please cite this article as: Salvatore Giovanni Michele Raccuia et al., *Journal of Industrial and Engineering Chemistry*, https://doi.org/10.1016/j.jiec.2025.09.008

are crucial for a variety of advanced technologies, including electronics (light-emitting diodes, lasers, electronic video displays, magnets), renewable energy systems and catalysts, highlighting the strategic importance of ensuring a stable supply. Traditional mining of REEs is often associated with environmental degradation and geopolitical uncertainties, thus requiring the exploration of alternative sources and sustainable extraction methods [2]. China, United States of America and Australia are the leading producers of rare earth elements, with China holding 90 % of the global production [3,4]. In the specific cases of neodymium (Nd) and dysprosium (Dy), their main applications include magnets (43.2 %), catalysts (17 %), polishing powders (11.2 %), metallurgy (7.1 %), glass (6.4 %), battery alloys (3.6 %), ceramics (3 %), phosphors (0.5 %), pigments (0.3 %), and other uses (7.6 %) [5]. Since the applications mentioned above are increasingly significant, and with the demand for REEs expected to grow in the future, it is essential to develop protocols aimed at their recovery and reuse. This will help reduce dependence on natural resources and lessen environmental impact. One of the primary strategies already being utilized is the so-called "green mining", which involves recovering resources from urban waste through the valorization of WEEEs (Waste of Electrical and Electronic Equipment), but currently only 1 % is being recycled [6]. This aligns with the key objectives of the European Green Deal and Energy Transition [7]. Unfortunately, the separation of REEs from WEEEs is a hard task. At present, the most used methods are based on mechanical and/or metallurgical treatments. Mechanical recycling works by separating various components based on size, density, and magnetic properties. Yet, this method is quite rough and is mainly applicable to WEEEs with a high REEs content, making it unsuitable for all types of e-waste. As for metallurgical processes, two primary methods are used: pyrometallurgy and hydrometallurgy. Pyrometallurgy involves heating WEEEs to high temperatures in the presence of a reducing agent, to obtain target metals in their elemental form. While effective, this process is highly energy consuming. Hydrometallurgy, on the other hand, involves two steps: first, leaching the e-waste with aqua regia, followed by LLE (Liquid-Liquid Extraction) and precipitation. This method allows the recovery of target metals from the solution in their oxidized form. Again, though highly efficient, it requires the employment of toxic and corrosive chemicals [3,8–10]. As a result, finding alternative strategies to overcome the main limitations of established methods (such as the use of toxic solvents in LLE and high energy costs) is of great importance and has become a hot topic in environmental chemistry research [11]. Literature indicates that one of the most explored strategies for recovering REEs from complex matrices is improving LLE. In this sense, emerging techniques include dispersive liquid–liquid extraction [12], solidified floating organic drop extraction [13] and extraction using ionic liquids [14]. Alternatively, the adsorption of REEs on various materials has been extensively studied. Examples include ionic exchange resins [15], task-specific polymers [16], and green adsorbents [17]. Additionally, various bio-based materials, both in their natural form and functionalized, have been investigated for this purpose [18–20]. Adsorption is considered one of the most promising technologies to separate metals and REEs from aqueous solutions [21]. Its appeal lies in its simplicity and the feasibility of using a wide range of adsorbents, resulting in cost-effective and sustainable processes. Moreover, adsorption offers advantages over LLE, including reduced waste and lower consumption of organic solvents. As a result, waste biomasses derived from agricultural and industrial processes have emerged as attractive candidates for sorption applications. These materials are abundant, underutilized (*e.g.*, for biofuel, pellet production, soil amendments, etc.), and inexpensive, with a high potential for effective removal of metal ions from aqueous solutions, offering the double benefit of waste reduction and resource extraction [22]. Basing on the above, this study investigates the adsorption capabilities of three distinct biomasses – BP (Bergamot Pomace), GP (Grape Pomace) and OP (Olive Pomace) – for the removal of $Nd^{3+}$ and $Dy^{3+}$ ions, two key REEs, from aqueous solutions. These biomasses were selected due to their local availability, composition, and surface chemistry properties. The pomaces underwent various pre-treatment methods to enhance their adsorption efficiency. Specifically, water pre-treatments were used to remove water-soluble molecules, whilst nitric acid pre-treatments were performed to eliminate alkaline ($Na^+$, $K^+$) and alkaline-earth ($Ca^{2+}$) metal cations [23]. ATR FT-IR (Attenuated Total Reflectance Fourier Transform Infrared) spectroscopy and SEM-EDX (Scanning Electron Microscopy – Energy Dispersive X-ray) analysis were employed to elucidate post-adsorption changes in functional groups. Notably, the potential of bergamot pomace for $Cd^{2+}$ adsorption was previously investigated by Irto *et al.* [24], demonstrating effective removal of this cation from aqueous solutions.

The effectiveness of biomasses in adsorbing neodymium(III), lanthanum(III), and dysprosium(III) ions from water and in the presence of $NaNO_3$ ionic medium was evaluated at various pHs through adsorption kinetics and isotherm studies. Additional tests were carried out in the presence of $La^{3+}$, enabling comparisons between light and heavy lanthanide ions. Additionally, the suitability of the biomasses for multiple adsorption/desorption cycles was investigated, highlighting their potential reusability through different loading/desorption cycles. This study reports, for the first time, the use of direct ITC (Isothermal Titration Calorimetry) to experimentally determine the enthalpy changes associated with the sorption of $Nd^{3+}$ and $Dy^{3+}$ onto BP. Unlike conventional determinations based on isotherm data collected at different temperatures and analyzed via the van't Hoff equation – a derivative method inherently prone to larger errors [25–28] – ITC enables a more accurate estimation of thermodynamic parameters. Although numerous studies have examined REEs biosorption on agricultural wastes, none have directly quantified sorption enthalpies using ITC, leaving key aspects of the interaction mechanisms unresolved. To fill this gap, the present work investigates the adsorption of $Nd^{3+}$ and $Dy^{3+}$ onto bergamot, grape, and olive pomaces, combining ITC measurements with adsorption modeling, life cycle assessment, and techno-economic analysis. While ITC has previously been applied to dye adsorption systems (e.g., methylene blue onto tangerine peel [29]), its application to REE biosorption remains unexplored. Lastly, LCA (Life Cycle Assessment) and TEA (Techno-Economic Assessment) analyses were also conducted to evaluate the sustainability, in terms of economic and environmental costs, of the BP use as biosorbent under different operational scenarios. Overall, this study demonstrates the potential of waste biomasses as eco-friendly, cost-effective, and scalable adsorbents for critical raw material recovery, contributing to circular economy strategies and sustainable resource management.

## Materials and methods

### *Materials and chemicals*

A 5 kg sample of bergamot pomace (*i.e.*, seeds, pulp and deoiled flavedo remaining after essential oil and juice extraction), from the *Femminello* and *Fantastico* cultivars, harvested between November 2021 and January 2022, was supplied by *Capua 1880* company (Reggio Calabria, Italy). A 6 kg sample of grape pomace (*i.e.*, seeds and pulp) from the 2023 harvest of the *Carricante* cultivar was provided by *Azienda Agricola "GIUSEPPE RUSSO"* (Passopisciaro, Catania, Italy). A 10 kg sample of olive pomace constituted by seeds and deoiled pulp post-olive oil extraction, from the *Nocellara dell'Etna* cultivar, harvested in 2022, was supplied by *Frantoio Russo* (Randazzo, Catania, Italy).

Portions of each pristine pomaces were mechanically ground, dried in an oven at $t = 60$ °C until constant weight, and then ground again to obtain a fine powder. An aliquot of the bergamot pomace was also freeze-dried. The resulting solid materials (referred to as RAW pomace) were divided in two fractions and pre-treated with either deionized water or standard solutions of nitric acid, the latter prepared by diluting Riedel–deHäen (Seelze, Germany) concentrated ampoules. These nitric acid solutions were also employed in desorption studies.

$La(NO_3)_3{\cdot}xH_2O$ (32–37 % La), $Nd(NO_3)_3{\cdot}6H_2O$ (32.0–33.7 % Nd) and $Dy(NO_3)_3{\cdot}xH_2O$ (34–37 % Dy) salts (Sigma Aldrich, Milan, Italy) were used for the preparation of the REEs solutions. Standard solutions of $La^{3+}$, $Nd^{3+}$ and $Dy^{3+}$ ions for instrumental calibration were prepared by diluting 1000 mg/dm$^3$ standard solutions of the REEs ions in 2 % $HNO_3$ (CPAchem, Bogomilovo, Bulgaria). $NaNO_3$ salt (purity ≥ 99.0 %, Sigma-Aldrich, Milan, Italy), previously dried in an oven at $t = 110$ °C for 2 h, was used for the preparation of ionic medium solutions.

*Pre-treatments of pomace samples*

RAW pomace samples (see Section 2.1) were either used directly or pre-treated exploiting different procedures already reported in the literature [23,24,30–32]. Specifically, weighed amounts of each biomass were put in contact with either deionized water or nitric acid solutions ($C_{HNO3} = 0.0983$ mol/dm$^3$) at $t = 30$ °C, using a solid-to-liquid ratio of 100 g/dm$^3$. Each mixture was centrifuged at 5000 rpm for 5 min at $t = 25$ °C to separate the solid from the liquid phases. The pH was measured by means of a 713-model pH meter equipped with a 6.0233.100 combined glass electrode (Metrohm, Herisau, Switzerland). Then, the supernatant was removed while the solid residues were washed with 25 cm$^3$ of deionized water, then centrifuged again. The pH was checked again, and the washing procedure repeated several times (generally 8 to 10 cycles), until the difference in pH between two consecutive washing cycles was less than 0.05 pH units. Subsequently, the solids residues were dried in an oven at $t = 60$ °C to constant weight (average yield *ca.* 40 %) and then mechanically ground to obtain a fine powder. A list of sorbent materials used in this study is given in Table 1.

*Material characterization*

Infrared spectra were obtained from the sorbent samples using a Nicolet iS50 FT-IR (Fourier Transform Infrared) spectrometer (Thermo Fisher Scientific, Waltham, Massachusetts, USA) equipped with an ATR (Attenuated Total Reflectance) diamond window module, operating in the middle infrared range (from 4000 to 400 cm$^{-1}$). Each spectrum was collected over 32 scans, with a spectral resolution of 4 cm$^{-1}$. Prior to analysis, the samples were ground to a fine powder using an agate mortar.

The microstructure of the biomasses was investigated using FESEM (Field-Emission Scanning Electron Microscopy) with a JEOL JSM-7610F Plus instrument (JEOL Ltd., Tokyo, Japan), operating at an accelerating voltage of 15 kV and a working distance of 15 mm. To enhance conductivity, samples were coated with a 5 nm layer of gold. The microscope was equipped with an EDXS (Energy-Dispersive X-ray Spectroscopy, Oxford Instruments) system for elemental analysis.

*Procedures for equilibrium, kinetic and recycle experiments*

Preliminary adsorption tests (*i.e.*, single batch) were conducted on the different pomace-based sorbents (Table 1) to identify the most promising pomace samples for the removal of $Nd^{3+}$ and $Dy^{3+}$ ions. In each test, approximately 10 mg of sorbent were added to 50 cm$^3$ Erlenmeyer flasks containing 20 cm$^3$ of REEs solution ($C_{REE} \sim 0.18$ mmol/dm$^3$) at $pH_i = 5.0$ (subscript "i" stands for initial value). Additional experiments at $pH_i = 3.0$ and 4.0 were performed for BP $H_2O$, GP $H_2O$, RAW OP. Suspensions were stirred for 24 h using an orbital mixer (model M201-OR, MPM Instruments, Bernareggio, Italy) placed in a thermostatted chamber (at $t = 25$ °C), and filtered using nylon syringe filters (SPHEROS, pore size = 0.45 μm). Then, the supernatants were collected to measure REE equilibrium concentration ($C_e$) by ICP-OES (Inductively Coupled Plasma-Optical Emission Spectrometry) using an Optima 2100 PerkinElmer instrument (Waltham, Massachusetts, USA), equipped with an autosampler (model AS-90A).

Batch isotherm experiments were carried out to test BP $H_2O$, RAW OP, and GP $H_2O$ sorption performances towards $Nd^{3+}$ and $Dy^{3+}$ at $pH_i = 5.0$ in 100 cm$^3$ Erlenmeyer flasks, using varying amounts of sorbent material (10–90 mg) and either 20 or 40 cm$^3$ of REEs solution ($0.18 \leq C_{REE}$/mmol dm$^{-3} \leq 0.36$). The ratio between milliequivalents of sorbent functional sites (estimated from preliminary tests) and metal cation ranged from approximately 1 to 10. All mixtures were stirred for 24 h and filtered as above reported. The supernatants were collected to determine the equilibrium pH ($pH_e$) using a Metrohm 713-pH meter equipped with a combined glass electrode (model 6.0233.100 from Metrohm, Herisau, Switzerland) and the equilibrium metal ion concentrations ($C_e$) as above reported. Due to its superior performance, BP $H_2O$ was further studied. In particular, additional isotherm experiments were conducted for $La^{3+}$, in conditions similar to those for $Nd^{3+}$, and $Dy^{3+}$. Moreover, further tests for all the three mentioned cations were also conducted in 0.10 mol/dm$^3$ sodium nitrate solutions (at $pH_i = 5.0$ and $t = 25$ °C).

The sorption capacity ($q_e$, in mmol/g) at different sorbent/metal ratios was calculated by means of Eq. (1):

$$q_e = \frac{V{\cdot}(C_0 - C_e)}{m} \quad (1)$$

where $V$ is the volume (in dm$^3$) of batch solutions, $C_0$ and $C_e$ are the initial and equilibrium metal cation concentration (in mmol/dm$^3$) and $m$ is the sorbent mass (in g).

Kinetic experiments were carried out at $pH_i = 5.0$ and $t = 25$ °C in a batch mode. Approximately 30 mg of sorbent were added to flasks containing 20 cm$^3$ of the $La^{3+}$, $Nd^{3+}$ or $Dy^{3+}$ solutions ($C_{REE} = 0.36$ mmol/dm$^3$). Suspensions were stirred at 180 rpm in an orbital mixer and subsequently filtered for solid-to-supernatant separation. Metal cation concentration in solution was measured at various contact times in a timeframe ranging from 0 to 2880 min. Sorption ability as a function of time ($q_t$, in mmol/g) was measured as for $q_e$ in Eq. (1), but equilibrium concentration $C_e$ was replaced by $C_t$ (Eq. (2)), namely the metal cation concentration measured at any time ($t$).

$$q_t = \frac{V{\cdot}(C_0 - C_t)}{m} \quad (2)$$

Sorbent reusability for $Nd^{3+}$ and $Dy^{3+}$ recovery was evaluated *via* column experiments. Approximately 20 mg of adsorbent were packed into a glass column (diameter = 2 cm, length = 10 cm). A 15 cm$^3$ metal solution ($C_{REE} = 0.18$ mmol/dm$^3$) was flowed at reflux into the column with a flow rate of 6 cm$^3$/min for 17 h using a peristaltic pump (Minipuls 3, Gilson, Cinisello Balsamo, Italy). Desorption was subsequently performed using a 0.10 mol/dm$^3$ $HNO_3$ solution for 7 h, followed by washing with 100 cm$^3$ of deionized water. Successive adsorption/desorption cycles were conducted under the same conditions. The solutions obtained from each adsorption/desorption step were collected and the metal concentration was determined to calculate both adsorption and desorption capacities.

**Table 1**
List of the different pomace-based sorbents tested.

| Pristine materials | Pre-treatment | Abbreviations | Symbol |
|---|---|---|---|
| Bergamot pomace | None | RAW BP | A |
| Bergamot pomace | Freeze-drying | BP LYO | B |
| Bergamot pomace | Freeze-drying + $H_2O$ at $t = 30$ °C | BP LYO $H_2O$ | C |
| Bergamot pomace | $H_2O$ at $t = 30$ °C | BP $H_2O$ | D |
| Bergamot pomace | $HNO_3$ at $t = 30$ °C | BP $HNO_3$ | E |
| Olive Pomace | None | RAW OP | F |
| Olive Pomace | $H_2O$ at $t = 30$ °C | OP $H_2O$ | G |
| Olive Pomace | $HNO_3$ at $t = 30$ °C | OP $HNO_3$ | H |
| Grape Pomace | None | RAW GP | I |
| Grape Pomace | $H_2O$ at $t = 30$ °C | GP $H_2O$ | J |
| Grape Pomace | $HNO_3$ at $t = 30$ °C | GP $HNO_3$ | K |

*Models for adsorption kinetic and isotherm experiments*

The experimental data of the REEs adsorption kinetics ($t$ and $q_t$) onto BP, OP and GP were fitted with different kinetic models, namely PFO (pseudo-first order, Eq. (3)), PSO (pseudo-second order, Eq. (4)), PGO (pseudo-n order, Eq. (5)), and DEM (double exponential model, Eq. (6)) equations [33–36]:

$$q_t = q_e \cdot \left(1 - e^{-k_1 \cdot t}\right) \quad \text{PFO} \tag{3}$$

$$q_t = \frac{q_e^2 + k_2 \cdot t}{1 + q_e \cdot k_2 \cdot t} \quad \text{PSO} \tag{4}$$

$$q_t = q_e \cdot \frac{q_e}{\left(1 + q_e^{(n-1)} \cdot k_n \cdot t \cdot (n-1)\right)^{\frac{1}{n-1}}} \quad \text{with } n \neq 1 \quad \text{PGO} \tag{5}$$

$$q_t = q_e\left[1 - \alpha \cdot e^{-kp_1 \cdot t} - (1-\alpha) \cdot e^{-kp_2 \cdot t}\right] \quad \text{with } 0 < \alpha \leq 1 \quad \text{DEM} \tag{6}$$

where $k_1$ (1/min), $k_2$ [g/(mmol·min)], $k_n$ [(1/min)(g·mmol)$^{(n-1)}$], $kp_1$ (1/min) and $kp_2$ (1/min) are the rate constants of adsorption according to the various models, n is the order of the PGO model, $a$ accounts for the relative contribution of each exponential term to the overall adsorption amount ($0 < \alpha < 1$) in the DEM model [37], whereas $q_t$ and $q_e$ were defined above.

Additionally, the Boyd model was employed to further investigate the mass transfer mechanism and to identify the rate-limiting step of the adsorption process [38]. This model helps distinguish whether external film diffusion or intraparticle diffusion governs the overall adsorption kinetics. The fractional attainment of equilibrium (F) was calculated using the following expression:

From the F values, the time-dependent Boyd function $B_t$ was derived using the following equations:

$$F = \frac{q_t}{q_e} \tag{7}$$

When $F \leq 0.85$

$$B_t = \left(\sqrt{\pi} - \sqrt{\pi - \frac{\pi^2 \cdot F}{3}}\right)^2 \tag{8}$$

When $F > 0.85$

$$B_t = ln\frac{\pi^2}{6} - ln(1-F) \tag{9}$$

The values of $B_t$ were then plotted as a function of time ($t$) to evaluate the linearity and intercept of the curve. According to the model, a linear plot of $B_t$ *vs.* $t$ that passes through the origin (the point with 0,0 co-ordinates) indicates that intraparticle diffusion is the rate-limiting step. Conversely, if the fitting line does not pass through the origin, film diffusion is the dominant mechanism controlling the adsorption rate [39].

The experimental data obtained from batch isotherm adsorption experiments ($C_e$ and $q_e$) were processed with Freundlich (Eq. (10)) and Langmuir (Eq. (11)) isotherm model equations [40–42]:

$$q_e = K_F \cdot C_e^{1/n} \tag{10}$$

$$q_e = \frac{q_m \cdot K_L \cdot C_e}{1 + K_L \cdot C_e} \tag{11}$$

where $K_F$ (dm$^{3/n}$·mmol$^{(1-1/n)}$/g) and $K_L$ (dm$^3$/mmol) are the affinity constants for the Freundlich and Langmuir models, respectively; $q_m$ is the maximum adsorption capacity (in mmol/g) according to the Langmuir model.

In order to evaluate the recovery and reuse performance of the biosorbents, adsorption–desorption cycles were performed and quantified. The adsorbed amount of REEs after each cycle was calculated using Eq. (1). The amount of metal desorbed during the regeneration phase was determined from the concentration of metal released in the acidic effluent:

$$q_{des} = \frac{V_{des} \cdot C_{des}}{m} \tag{12}$$

The recovery efficiency (R%) for each cycle was then calculated as:

$$R(\%) = \frac{q_{des}}{q_e} \cdot 100 \tag{13}$$

These values were used to track both the stability of the material and the effectiveness of REE recovery over successive reuse cycles.

*Calorimetric measurements*

With the aim of investigating the thermodynamic parameters of the sorption process, ITC experiments were carried out at $t = 25.0000 \pm 0.0001$ °C using a TAM III thermostat (TA Instruments, New Castle, Delaware, USA) equipped with a nanocalorimeter (1 cm$^3$ cell volume) and an automatic titration Hamilton syringe of 0.25 cm$^3$. The TAM III device is featured by two stainless steel cells: one designed for the sample and the other for the reference (*i.e.*, deionized water and 10 mg of BP). Each titration experiment consisted of ten consecutive injections of 0.01 cm$^3$ of $Nd^{3+}$ or $Dy^{3+}$ aqueous solution ($C_{Nd} = 0.0540$ mol/dm$^3$; $C_{Dy} = 0.0538$ mol/dm$^3$) into 0.75 cm$^3$ of deionized water containing a weighed sorbent amount (approx. 10 mg). The blank experiments were performed by injecting the REEs cation solutions into 0.75 cm$^3$ of deionized water in the absence of the biosorbent. A delay time of 60 mins was set between two consecutive injections. The sample cell was stirred constantly at 50 rpm using a gold helix.

The adsorption enthalpy change ($\Delta_{sor}H$) was calculated by Eq. (14):

$$\Delta_{sor}H = \frac{(q_{i,sor} - q_{dil})}{n_i} \tag{14}$$

where: $q_{i,sor}$ is the heat measured during the titration experiment as a consequence of the REE sorption by the material, $q_{dil}$ is the dilution heat, obtained from the titration of $Ln^{3+}$ solutions in water, and $n_i$ is the number of moles of $Ln^{3+}$ adsorbed after each injection, calculated from the parameters of the isotherm model equation.

The free Gibbs energy ($\Delta_{sor}G$) and entropy ($\Delta_{sor}S$) changes for $Nd^{3+}$ and $Dy^{3+}$ adsorption processes were calculated using the following equations (Eqs. (15) and (16)):

$$\Delta_{sor}G = -R \cdot T \cdot \ln K_C = -R \cdot T \cdot \ln(55.5 \cdot 1000 \cdot AM \cdot K_L) \tag{15}$$

$$\Delta_{sor}S = (\Delta_{sor}H - \Delta_{sor}G)/T \tag{16}$$

where $R$ is the universal gas constant ($R = 8.314$ J/(mol·K)), $T$ is the temperature in Kelvin (K) scale, $K_C$ is a dimensionless sorption parameter, 55.5 is the number of pure water moles for each liter, AM is the atomic mass (g/mol) of each lanthanide, $K_L$ is the Langmuir affinity constant (see Eq. (11)) converted in dm$^3$/mol using a 1000 conversion factor [29,42].

*Life Cycle Assessment (LCA) and Techno-Economic Assessment (TEA)*

A Life Cycle Assessment was conducted according to ISO 14040 [43] and ISO 14044 [44] standards to evaluate the environmental profile of BP $H_2O$. The functional unit was defined as 1 kg of biosorbent produced. A gate-to-gate system boundary was used, including feedstock preparation, manufacturing, regeneration. Being an agrowaste, the production of raw BP was excluded from the analysis. The end-of-life phase, transportation, and lab infrastructure impacts were excluded from the system boundaries due to the localized, bench-scale nature of the system, consistent with LCA practices for early-stage processes [45,46].

Inventory data, detailed in Table 2, were obtained from lab measurements and supplemented by the Ecoinvent v3 database [47]. The environmental impacts were assessed using SimaPro software, applying the ReCiPe 2016 Midpoint method (H), focusing on the most relevant areas of the system: GW (Global warming, in kg $CO_2$ eq), WC (Water Consumption, in $m^3$), and CED (Cumulative Energy Demand, in MJ). In addition to the lab-scale scenario, three alternative scenarios were modelled: S1 with improved drying efficiency of 0.7 kWh/kg [48], S2 performing four regeneration cycles with acidic desorption, and S3 combining both efficient drying and regeneration. To support the environmental analysis, a preliminary TEA was conducted within the same boundaries as the LCA to estimate production costs. The analysis focused solely on upstream and processing stages, excluding labor costs, which are often uncertain at early research and development stages [49]. Cost estimation considered direct expenses related to raw materials, energy use, and consumables, expressed per unit of functional output, defined as 1 kg of dried biosorbent. Electricity costs were estimated based on the average supply costs to non-domestic customers, at 0.30 €/kWh [50]; deionized water costs were estimated from the laboratory inventory, 60 € for 1000 $dm^3$ filter, or 0.06 €/$dm^3$; nitric acid costs were 100 € for 1 $dm^3$ of 10 mol/$dm^3$ nitric acid solution, or 0.5 €/0.1 mol/$dm^3$ [51]. Sensitivity analyses aligned with those of the LCA were performed to facilitate comparison of environmental and economic performance. This limited-scope TEA offers an initial indication of the process' economic feasibility and highlights potential routes for future process optimization and scaling up [52].

This table summarizes the Life Cycle Inventory of lab-scale production of BP $H_2O$ **(B1)**, with S1 using a more efficient drying process, S2 regenerating the Spent BP $H_2O$ over 4 adsorption–desorption cycles with a 9 % efficiency drop from the first to the fourth cycle, and S3 performing both efficient drying and regeneration. A flow diagram of the system boundaries and life cycle stages across the four scenarios considered is given in Fig. S1.

## Results and discussion

### *Preliminary adsorption tests*

The results obtained from preliminary tests, in terms of measured $q_e$, at pHi = 5.0 are shown in Fig. 1 and the numerical values of measured $q_e$ for each test are listed in Table S1. The RAW bergamot pomace samples – whether oven-dried (BP RAW) or freeze-dried (BP LYO) – exhibited limited adsorption capacities for $Nd^{3+}$ and $Dy^{3+}$, with the freeze-dried ones performing the poorest. In contrast, water pre-treated samples (BP LYO $H_2O$, and BP $H_2O$) demonstrated a notable improvement in adsorption capacity compared to raw counterparts. Between the two dehydration techniques tested, freeze-drying and thermal, the latter performed better for sorption of both metal cations. The pre-treatment with $HNO_3$ also proved to be effective for increasing sorption capacity, however the corresponding $q_e$ values ($q_e \sim 0.22$ mmol/g) were lower than those recorded for the $H_2O$-treated counterparts ($q_e \sim 0.27$ mmol/g). In the case of grape pomace, the RAW biomass displayed lower $q_e$ values ($q_e \sim 0.10$ mmol/g) than the $H_2O$-treated samples ($q_e \sim 0.11$ mmol/g), yet higher than those pre-treated with nitric acid ($q_e \sim 0.09$ mmol/g), with both metal cations. Olive pomace, on the other hand, exhibited good adsorption performance as RAW material ($q_e \sim 0.15$ mmol/g), but the $q_e$ value decreased for samples pre-treated with either $H_2O$ or $HNO_3$.

**Table 2**
Life Cycle Inventory of lab-scale production of BP $H_2O$.

| Input | B1 | S1 | S2 | S3 | Unit |
|---|---|---|---|---|---|
| Raw Bergamot Pomace | 4.16 | 4.16 | 1.04 | 1.04 | Kg |
| Drying electricity consumption | 11.96 | 1.4 | 3 | 0.35 | kWh |
| Grinding electricity consumption | 0.023 | 0.023 | 0.006 | 0.006 | kWh |
| Centrifuge electricity | 0.14 | 0.14 | 0.035 | 0.035 | kWh |
| Distilled water | 166.66 | 166.6 | 41.67 | 41.67 | $dm^3$ |
| Nitric acid (0.1 mol/$dm^3$) | 0 | 0 | 0.75 | 0.75 | $dm^3$ |
| **Output** | | | | | |
| BP $H_2O$ | 1 | 1 | 1 | 1 | kg |

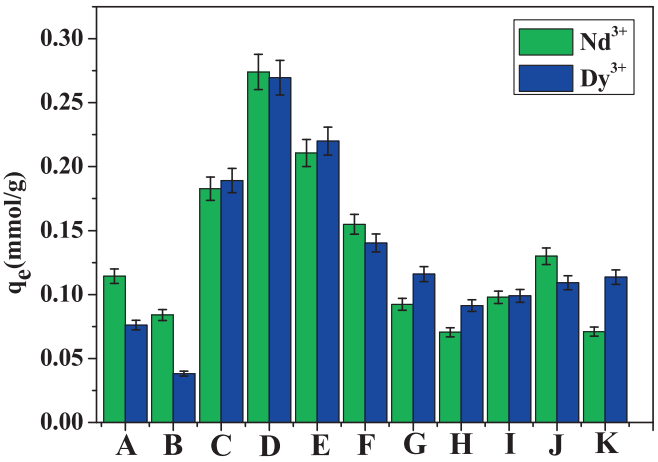


**Fig. 1.** Screening of the sorption capacity of all the tested BP (A-E), GP and OP-based materials towards $Nd^{3+}$ and $Dy^{3+}$.

The differences in adsorption performance among bergamot, grape, and olive pomaces can be likely attributed to their overall chemical composition and surface acid–base properties. Bergamot pomace is richer in polysaccharides bearing carboxyl and hydroxyl groups, which are known to promote the interaction with REE cations through complexation and ion-exchange mechanisms. In contrast, grape and olive pomaces contain higher proportions of lignin and phenolic moieties, which may hinder the accessibility or reactivity of such functional groups [23,53,54].

These trends are consistent with potentiometric titration data previously reported in our earlier work [23], in which the concentration of surface carboxylic groups was quantified to be 1.10 ± 0.02 meq/g for BP $H_2O$, 0.23 ± 0.01 meq/g for GP $H_2O$, and 0.21 ± 0.01 meq/g for OP $H_2O$. The higher abundance of carboxylic groups in BP $H_2O$ likely contributes to its superior adsorption capacity observed in Fig. 1. Based on the outcomes of the preliminary adsorption tests, one sorbent sample was selected for each pristine material. Accordingly, BP $H_2O$, GP $H_2O$, and RAW OP were identified as the best-performing materials and subsequently tested further. In particular, to assess the best pH conditions for REE adsorption, single-batch experiments were also carried out at $pH_i = 3.0$ and $pH_i = 4.0$. The results are summarized in Fig. 2, in which the data at $pH_i = 5.0$ are those already reported in Fig. 1. The results showed that the adsorption capacity increased as the initial pH ($pH_i$) increases. This behavior could be attributed to the competition between REE cations and $H^+$ ions for the binding to active sorption sites. At $pH_i = 3.0$, the high concentration of $H^+$ ions significantly hindered REE uptake, reducing the adsorption efficiency of the tested material. Conversely, the highest adsorption capacity for $Nd^{3+}$ and $Dy^{3+}$ was observed at $pH_i = 5.0$, which was therefore selected as the optimal pH condition for further adsorption isotherm experiments.

### *Spectroscopic and morphological investigations*

ATR FT-IR analysis was employed to identify the functional groups in BP $H_2O$, GP $H_2O$, and RAW OP potentially involved in the adsorption of $Nd^{3+}$ and $Dy^{3+}$.

The spectra of these materials were previously discussed in detail [23,24]. In particular, the FT-IR profiles exhibited broad bands at 3310–3330 $cm^{-1}$, corresponding to O–H stretching [55], and a weak

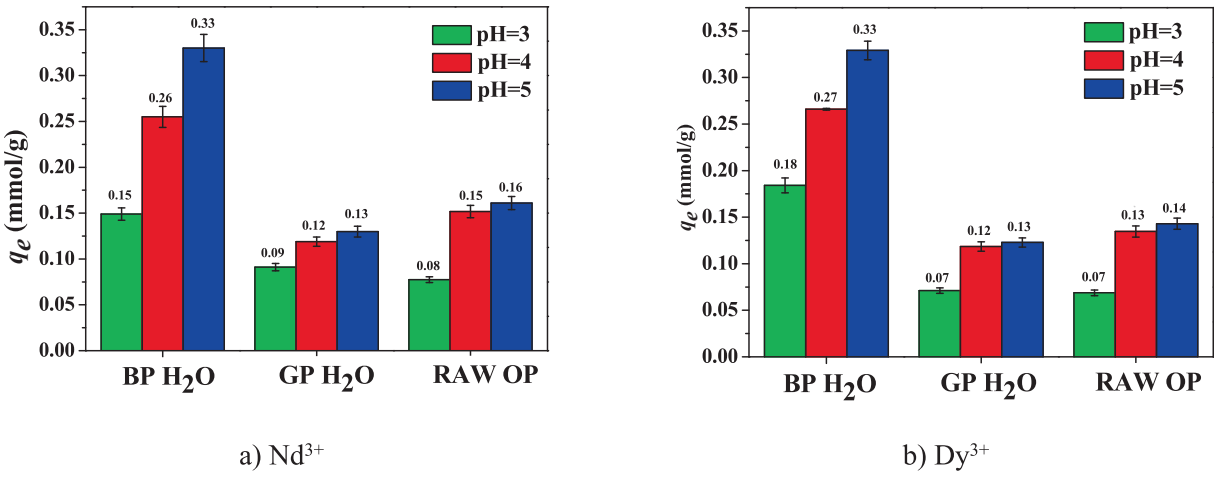


**Fig. 2.** $q_e$ values of $Nd^{3+}$ (a) and of $Dy^{3+}$ (b) adsorption onto BP $H_2O$, GP $H_2O$ and RAW OP in aqueous solution, at $pH_i = 3.0$, 4.0 and 5.0 at $t = 25$ °C. Experimental conditions: ~0.01 g of adsorbent in 20 $cm^3$ of REEs solution ($C_{REE}$ ~ 0.18 mmol/$dm^3$).

peak at 3010 $cm^{-1}$ attributed to aromatic C–H stretching [56]. Bands at ~2920 and 2850 $cm^{-1}$ were assigned to methylene and methyl stretching vibrations [57]. A band in the 1710–1740 $cm^{-1}$ range was attributed to C═O stretching of non-ionic carboxylic groups [58]. The peaks at ~1610–1650 and 1420–1440 $cm^{-1}$ were assigned to the asymmetric and symmetric stretching modes of carboxylates [23]. Bands at 1510–1526 $cm^{-1}$ were associated with aromatic C–C ring vibrations, characteristic of polyphenols [59]. Weak bands in the 1310–1350 $cm^{-1}$ region were attributed to C–O bending vibrations of methylene and alcoholic groups [60]. Finally, a weak band at 1230 and a more intense band at 1030 $cm^{-1}$ were assigned to C–O, O–C–O, and C–O–C stretching, as well as –$CH_2$ bending vibrations modes [24,61].

The infrared spectrum of BP $H_2O$ is reported in Fig. 3 before (black line) and after adsorption of $Nd^{3+}$ (blue line) and $Dy^{3+}$ (red line). Similar spectral comparisons for the other biomasses are given in the Supporting Information (Fig. S2).

After $Nd^{3+}$ and $Dy^{3+}$ sorption (Figs. 3 and S2), the three materials exhibited variations in the intensity of bands mainly associated to O–H, C–H, C═O, $COO^-$ and C–O–C vibrational modes, in accordance with Lapo and coworkers findings [19], who investigated the interactions of

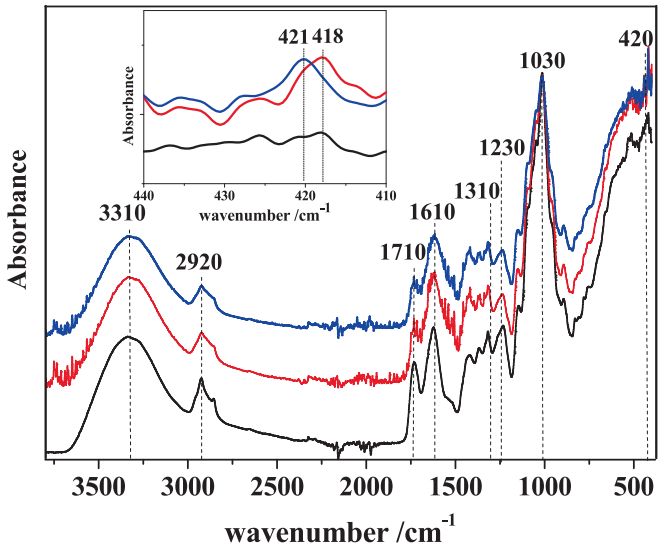


**Fig. 3.** ATR FT-IR spectra of BP $H_2O$ before (black line, [24]), and after sorption with $Nd^{3+}$ (blue line), and $Dy^{3+}$ (red line). (For interpretation of the references to colour in this figure legend, the reader is referred to the web version of this article.)

banana wastes and peels with various lanthanide ions, such as $Nd^{3+}$, $Dy^{3+}$, $Eu^{3+}$, and $Tb^{3+}$. Additionally, the sorption process induced shifts in the wavenumber (υ, in $cm^{-1}$) of maxima for bands attributed to both non-ionic and ionic carboxylic groups. The observed shifts ($\Delta\upsilon = \upsilon_{REE+biomass} - \upsilon_{biomass}$) ranged between 3 and 12 $cm^{-1}$, suggesting a possible involvement of these functional groups in the adsorption process, a hypothesis in line with Torab-Mostaedi *et al.* [28,62] who studied the La(III) and Ce(III) adsorption by orange and grapefruit peels. Comparable shifts were also reported by Yushin *et al.* [63] for $Er^{3+}$ adsorption onto *Arthospira platensis*, and Oliveira *et al.* [64], who examined interactions between $COO^-$ groups in *Sargassum* sp.-based adsorbents, and La(III), Nd(III), Eu(III), Gd(III) ions. They also introduced the Δ parameter, defined as the difference between the asymmetric ($\upsilon_{a(COO-)}$) and symmetric ($\upsilon_{s(COO-)}$) stretching wavenumbers, in the range of 213–216 $cm^{-1}$ for REE-carboxylate complexes. In the case of BP $H_2O$ (Fig. 3) and RAW OP (Fig. S2b) samples, comparable shift values (Δ = 200–230 $cm^{-1}$) were determined. In addition, the bergamot-based materials spectra showed an increase in the relative intensity ratios of the intensity the peaks at ~1619–1650 and ~1730–1735 $cm^{-1}$, as a further possible consequence of the BP $H_2O$-metal cations interaction. Specifically, the calculated $\upsilon_{a(COO-)}/\upsilon_{(COOH)}$ ratios were 1.70 and 1.75 with $Nd^{3+}$ and $Dy^{3+}$, respectively, compared to 1.36 in the absence of $M^{3+}$. Furthermore, the presence of new bands, as shown in the inset of Fig. 3, was observed in the samples recorded after the sorption of $Nd^{3+}$ (at ~421 $cm^{-1}$) and $Dy^{3+}$ (at ~418 $cm^{-1}$). These bands were attributed to stretching vibrations associated with the coordination of rare earth ions to the biosorbent surface functional groups [19,65].

To investigate morphological changes, the surface of BP $H_2O$, GP $H_2O$, and RAW OP were analyzed by SEM-EDX before and after REEs adsorption at a magnification of 1000 x. As shown in Fig. 4a, the BP $H_2O$ displayed a rough and heterogeneous surface, with fibrous and porous structures typical of lignocellulosic biomass. EDX analysis confirmed the presence of only carbon and oxygen. After $Nd^{3+}$ adsorption (Fig. 4b), SEM images revealed a smoother and more compact surface, suggesting interaction between neodymium and surface functional groups. EDX analysis confirmed the presence of $Nd^{3+}$ through its characteristic peaks (~1.0, 4.2, and 5.2 keV). For $Dy^{3+}$ adsorption (Fig. 4c), the BP surface appeared less altered than that of the BP-Nd sample, retaining visible fibrillar features. However, EDX spectra clearly showed $Dy^{3+}$ peaks (~1.0, 6.5, and 7.8 keV), confirming effective ion adsorption. Similar morphological changes and elemental signals were also observed for RAW OP and GP $H_2O$, as reported in the Supplementary Figs. S3 and S4, respectively. These findings confirmed the ability of both biomasses mentioned above to be used as sorbent materials for both $Nd^{3+}$ and $Dy^{3+}$ ions, with the former generally inducing more pronounced surface

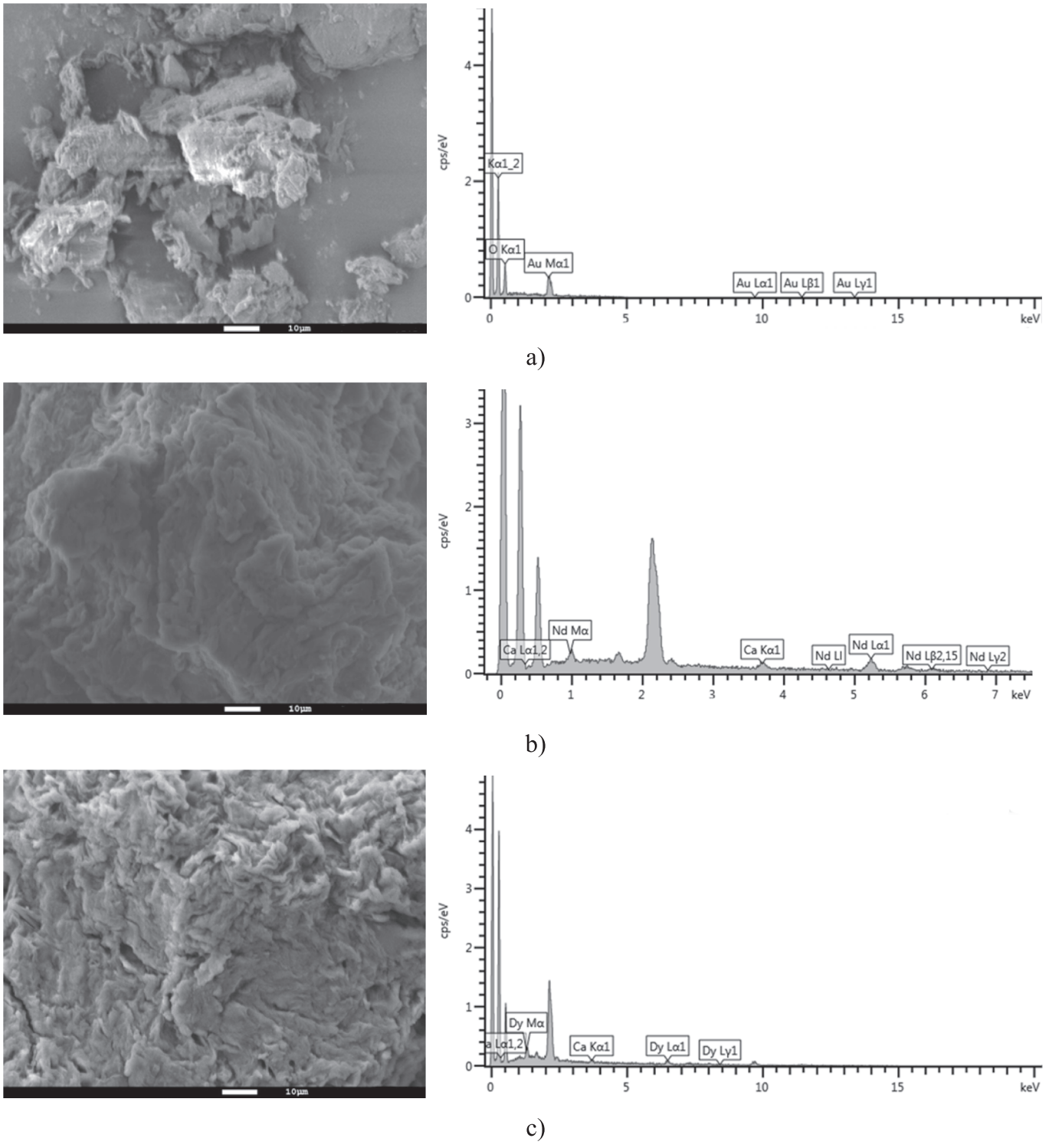


**Fig. 4.** SEM images of a) BP $H_2O$ before adsorption experiments and after adsorption of b) Nd, c) Dy. On the right the elemental analysis.

modifications [19].

*Adsorption kinetics*

The adsorption kinetics of $Nd^{3+}$ and $Dy^{3+}$ ions onto BP $H_2O$, RAW OP and GP $H_2O$ was investigated in the absence of ionic medium. The experimental data ($t$ and $q_t$) were analyzed using five kinetic models, namely PFO (Eq. (3)), PSO (Eq. (4)), PGO (Eq. (5)), DEM (Eq. (6)), and Boyd (Eqs. (7)–(9)). The results obtained with the five models were compared based on their fitting parameters, to identify which best reproduced the experimental data. As the PSO model provided the best fitting performances, the results obtained with this model, including the rate constant ($k_2$), equilibrium adsorption capacity ($q_e$), and fitting statistics ($R^2$ and RMSE), are reported in Table 3. The corresponding values for the PFO, PGO, DEM and Boyd models are reported in Tables S2–S5, respectively. Although the PSO model consistently provided better correlation coefficients ($R^2 > 0.98$) and more accurate predictions of $q_e$, the PFO model was included for comparison purposes, as it remains

**Table 3**
Parameters of PSO kinetic equation for the adsorption of $Nd^{3+}$ and $Dy^{3+}$ from aqueous solutions at $pH_i = 5.0$ and t = 25 °C.

| $M^{3+}$ | Adsorbent | $q_e$[a] | $k_2$[b] | $R^2$ | RMSE[c] |
|---|---|---|---|---|---|
| $Nd^{3+}$ | RAW OP | 0.11 ± 0.01 | 18 ± 4 | 0.9850 | 0.0047 |
| | GP $H_2O$ | 0.08 ± 0.01 | 8 ± 1 | 0.9837 | 0.0037 |
| | BP $H_2O$ | 0.32 ± 0.03 | 0.29 ± 0.03 | 0.9929 | 0.0073 |
| $Dy^{3+}$ | RAW OP | 0.12 ± 0.01 | 17 ± 3 | 0.9863 | 0.0047 |
| | GP $H_2O$ | 0.09 ± 0.01 | 4 ± 1 | 0.9848 | 0.0027 |
| | BP $H_2O$ | 0.25 ± 0.01 | 0.70 ± 0.10 | 0.9839 | 0.0117 |
| $La^{3+}$ | BP $H_2O$ | 0.29 ± 0.04 | 0.32 ± 0.01 | 0.9739 | 0.0165 |

[a] mmol/g ± std. dev.
[b] g/(mmol·min) ± std. dev.
[c] Root Mean Square Error, mmol/g.

widely reported in biosorption literature for rare earth elements [19,38,50]. However, the PFO model is generally more appropriate for systems governed by simple physisorption or initial diffusion-controlled uptake mechanisms. Scatter plots comparing the experimental and fitted data using the PSO model are displayed in Fig. 5, while those obtained from the other kinetic models are shown in Figs. S5–S9.

In many cases, the PSO model exhibited the best fitting performance. For example, for $Nd^{3+}$ adsorption onto BP $H_2O$, correlation coefficients were $R^2 = 0.9819$, 0.9929, 0.9915, and 0.9807 for PFO, PSO, PGO, and DEM, respectively. Similar trends were observed for RMSE values, which were 0.0118, 0.0073, 0.0079, and 0.0094, respectively. In other cases (e.g., $Dy^{3+}$ on BP $H_2O$), the PGO and DEM models showed good statistical parameters; however, the strong correlation between parameters in these models often led to unreliable estimates (*e.g.*, $kp_1 = 0.05 \pm 0.07$ 1/min, Table S4), thus limiting their applicability to our system. The analysis through the Boyd model revealed that, although none of the systems displayed perfect linearity, the regression lines did not pass through the origin, which strongly suggests that intraparticle diffusion cannot be considered the sole rate-limiting mechanism. Specifically, for $Nd^{3+}$ and $La^{3+}$ adsorption onto BP $H_2O$, moderate correlations were observed, with $R^2$ values of 0.788 and 0.789, respectively, and non-zero intercepts of 0.13 ± 0.06 and 0.19 ± 0.09. Similarly, $Dy^{3+}$ on BP $H_2O$ showed an $R^2$ of 0.616 with an intercept of 0.15 ± 0.05. For the other biosorbents, lower $R^2$ values were obtained *e.g.*, 0.391 for $Nd^{3+}$ on OP RAW and 0.397 for $Nd^{3+}$ on GP $H_2O$ and the intercepts were consistently non-zero. These results point to external film diffusion as the predominant mass transfer limitation, rather than intraparticle diffusion, across all tested systems.

This interpretation is consistent with recent findings reported in literature, where Boyd modeling applied to multicomponent systems also indicated film diffusion as the controlling step, even under competitive adsorption conditions [39].

A visual inspection of Figs. 5 and S5–S8 confirms that PFO was generally inadequate, whereas PSO can be regarded as the most suitable model for describing REE adsorption kinetics on the tested biosorbents. For both $Nd^{3+}$ and $Dy^{3+}$ ions, equilibrium was reached within 20 min on RAW OP and GP $H_2O$, with a rapid initial uptake followed by a slower plateau region. This two-step kinetic behavior is typical for adsorption processes and has been observed in numerous studies [18,26,28,62,66–69], where the initial phase corresponds to the availability of abundant active sites, and the later stage reflects site saturation and possible diffusional limitations [62]. In contrast, the BP $H_2O$ sample required a longer equilibrium time (ca. 120 min) and showed the lowest $k_2$ values among the tested biosorbents (Table 3). These findings were further confirmed by kinetic tests conducted with $La^{3+}$ under identical conditions. Also in this case, the data were best fitted by the PSO model (Fig. S8), although the $k_2$ value for $La^{3+}$ on BP $H_2O$ was lower than those observed for $Nd^{3+}$ and $Dy^{3+}$ adsorption on OP RAW and GP $H_2O$. The $k_2$ values obtained in this study for $La^{3+}$, $Nd^{3+}$, and $Dy^{3+}$ on BP $H_2O$ were 0.32, 0.29, and 0.70 g/(mmol·min), respectively (Table 3). The trend among the $k_2$ values may be related to differences in ionic radii of the REE ions: 1.045 Å ($La^{3+}$), 0.983 Å ($Nd^{3+}$), and 0.912 Å ($Dy^{3+}$) [70]. The smaller radius of $Dy^{3+}$ could enhance its mobility and affinity toward the active sites on the biosorbent surface, explaining the higher adsorption rate. This was further supported by comparisons of $k_2$ values with literature data on rare earth adsorption onto various biomasses [11,26,62,67–69,71–75], reported in Table 4. Despite the slower

**Table 4**
Pseudo-second-order rate constants ($k_2$) for rare earth adsorption onto various lignocellulosic biosorbents.

| Adsorbent | REE | $k_2$[a] | Ref. |
|---|---|---|---|
| BP $H_2O$ | $Nd^{3+}$ | 0.29 | This work |
| BP $H_2O$ | $Dy^{3+}$ | 0.70 | This work |
| BP $H_2O$ | $La^{3+}$ | 0.32 | This work |
| Banana waste | $Nd^{3+}$ | 0.027 | [19] |
| Banana peel | $Dy^{3+}$ | 0.019 | [19] |
| Orange peel | $La^{3+}$ | 0.017 | [28] |
| Grapefruit peel | $Ce^{3+}$ | 0.020 | [62] |
| Grape stalk | $La^{3+}$ | 0.008 | [11] |

[a] g/(mmol·min) ± std. dev.

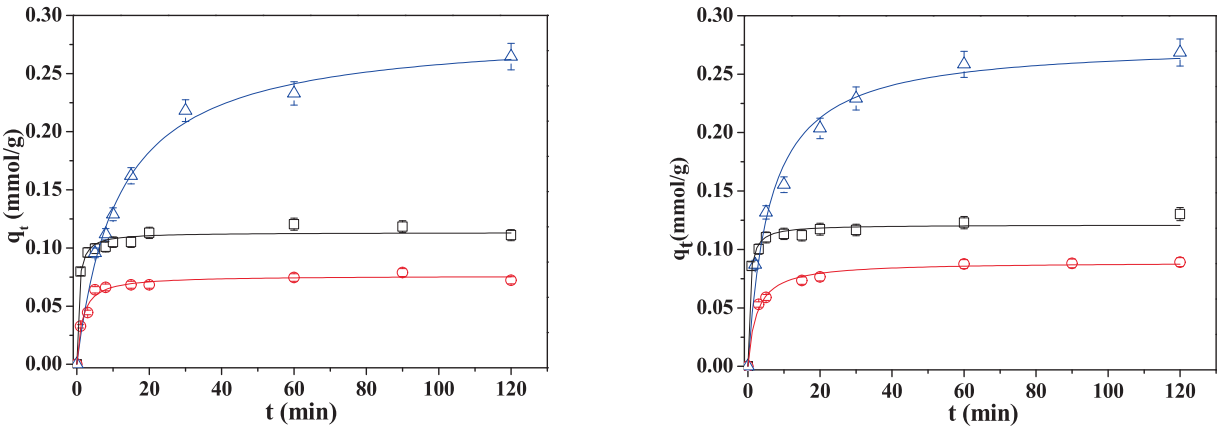


**Fig. 5.** PSO kinetics of adsorption of $Dy^{3+}$ (a) and $Nd^{3+}$ (b) ions on BP $H_2O$ (△), RAW OP (□), and GP $H_2O$ (○) samples.

kinetics of BP $H_2O$ compared to OP and GP in this study, its $k_2$ values remain higher than those reported for other unmodified lignocellulosic biosorbents [11,19,28,62]. For example, the pseudo-second-order rate constants ($k_2$) for BP $H_2O$ are 0.29, 0.70, and 0.32 g/(mmol·min) for $Nd^{3+}$, $Dy^{3+}$, and $La^{3+}$, respectively, whereas $k_2$ values reported for banana peel and orange peel range from 0.017 to 0.027 g/(mmol·min) [19,28]. These results highlight the relatively fast adsorption kinetics of BP $H_2O$ under the tested conditions, making it a promising candidate for practical application in continuous flow systems. While engineered sorbents show higher capacities, the use of unmodified fruit pomace offers clear advantages in terms of waste valorization, cost, and environmental impact, as also highlighted in the LCA and TEA sections.

*Adsorption isotherms*

The adsorption equilibria of $Nd^{3+}$ and $Dy^{3+}$ ions onto BP $H_2O$, RAW OP, and GP $H_2O$ were first studied in aqueous solutions at $pH_i = 5.0$, at low ionic strength and $t = 25$ °C. The collected data ($q_e$ *vs.* $C_e$) were subjected to regression analysis by both the Langmuir and Freundlich isotherm equations. Diagrams reporting scatter plots and corresponding lines representing the two isotherm equation models are depicted in Fig. 6, whereas the fitting parameters for the Langmuir and Freundlich models are collected in Table 5 and Table S6, respectively.

As a preliminary observation, the best fit was achieved by means of the Langmuir model. Although the strongest agreement with a specific isotherm model does not necessarily indicate the uptake mechanism of the REE ions, analysing the isotherm parameter values serves as a valuable tool for predicting and optimizing sorption processes. Considering the $q_m$ data (0.38 mmol/g for $Nd^{3+}$, 0.45 mmol/g for $Dy^{3+}$, Table 5) at $pH_i = 5.0$, BP $H_2O$ resulted to be the best adsorbent material for both the $Ln^{3+}$ ions, followed by RAW OP and GP $H_2O$ for Nd(III), by GP $H_2O$ and RAW OP for Dy(III), respectively. The highest adsorption capacity of the water-treated bergamot pomace could be attributed to its acid-base properties, as already discussed in a previous work [23]. Indeed, among the tested materials, BP $H_2O$ showed the highest acidity, with a protonation constant value of $\log^T K^H = 3.65$ at $t = 25$ °C, compared to 4.30 and 4.29 for GP $H_2O$ and RAW OP, respectively, in all the cases consistent with the presence of carboxylic groups [23]. Furthermore, the concentration of these active sites is higher in BP $H_2O$ (1.10 meq/g) with respect to GP $H_2O$ (0.23 meq/g) and RAW OP (0.43 meq/g). Consequently, under the investigated conditions, BP $H_2O$ likely exhibited the highest abundance of ionized carboxyl groups, potentially enhancing their interaction with REE ions.

In addition, as shown in Table 5, at $pH_i = 5.0$ RAW OP exhibits the

**Table 5**
Langmuir isotherm parameters for the $Nd^{3+}$, $Dy^{3+}$ and $La^{3+}$ ions from aqueous solutions adsorption onto RAW OP, GP $H_2O$ and BP $H_2O$ at t = 25 °C, $pH_i = 3.0$ to 5.0, low ionic strength (absence of ionic medium) and in $NaNO_3$ 0.10 mol/$dm^3$.

| $M^{3+}$ | Adsorbent | $pH_i$[a] | $pH_e$[b] | $q_m$[c] | $K_L$[d] | $R^2$ | RMSE[e] |
|---|---|---|---|---|---|---|---|
| $Nd^{3+}$ | RAW OP | 5.0 | 4.1 | 0.18 ± 0.01 | 48 ± 6 | 0.9905 | 0.0054 |
| | GP $H_2O$ | 5.0 | 4.0 | 0.17 ± 0.01 | 11 ± 2 | 0.9835 | 0.0052 |
| | BP $H_2O$ | 5.0 | 3.4 | 0.38 ± 0.01 | 27 ± 3 | 0.9915 | 0.0105 |
| | BP $H_2O$ | 5.0[f] | 3.6 | 0.16 ± 0.02 | 16 ± 4 | 0.9723 | 0.0079 |
| $La^{3+}$ | BP $H_2O$ | 5.0 | 3.6 | 0.35 ± 0.01 | 38 ± 4 | 0.9927 | 0.0100 |
| | BP $H_2O$ | 5.0[f] | 3.4 | 0.21 ± 0.01 | 20 ± 4 | 0.9757 | 0.0105 |
| $Dy^{3+}$ | RAW OP | 5.0 | 4.1 | 0.14 ± 0.01 | 81 ± 17 | 0.9699 | 0.0076 |
| | GP $H_2O$ | 5.0 | 4.0 | 0.16 ± 0.01 | 17 ± 6 | 0.9240 | 0.0106 |
| | BP $H_2O$ | 5.0 | 3.2 | 0.45 ± 0.02 | 12 ± 1 | 0.9912 | 0.0112 |
| | BP $H_2O$ | 5.0[f] | 3.4 | 0.16 ± 0.02 | 30 ± 10 | 0.9134 | 0.0167 |
| $Nd^{3+}$ | BP $H_2O$ | 4.0 | 3.3 | 0.28 ± 0.01 | 130 ± 20 | 0.9793 | 0.0121 |
| $Dy^{3+}$ | BP $H_2O$ | 4.0 | 3.6 | 0.29 ± 0.02 | 90 ± 20 | 0.9372 | 0.0211 |
| $Nd^{3+}$ | BP $H_2O$ | 3.0 | 2.9 | 0.24 ± 0.01 | 70 ± 30 | 0.9941 | 0.0069 |
| $Dy^{3+}$ | BP $H_2O$ | 3.0 | 2.9 | 0.18 ± 0.01 | 400 ± 100 | 0.9891 | 0.0066 |

[a] initial pH value of REE ions solutions.
[b] mean pH value at adsorption equilibrium.
[c] in mmol/g ± std. dev.
[d] in $dm^3$/mmol ± std. dev.
[e] Root Mean Square Error.
[f] adsorption isotherm carried out in $NaNO_3$ 0.10 mol/$dm^3$.

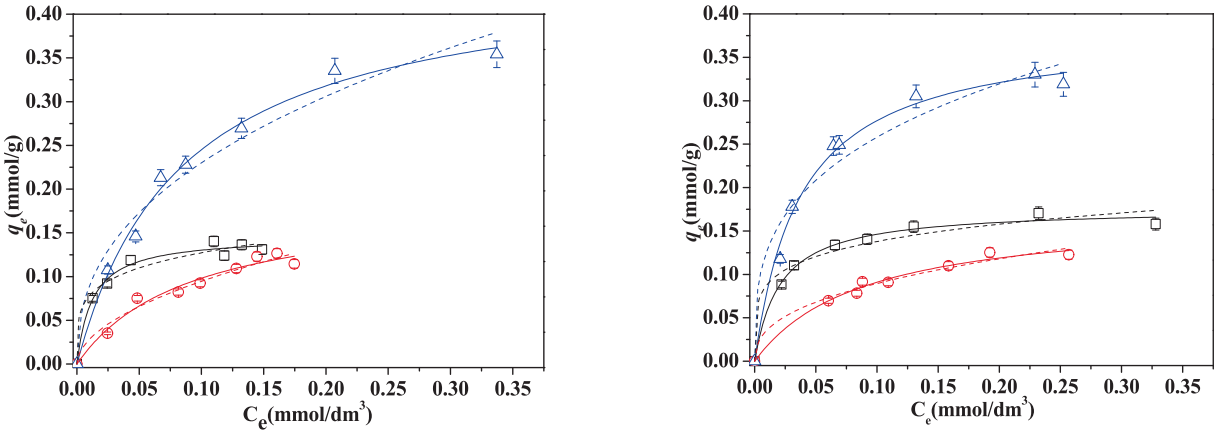


a) $Dy^{3+}$ b) $Nd^{3+}$

**Fig. 6.** Adsorption isotherms of $Dy^{3+}$ (a) and $Nd^{3+}$ (b) ions onto BP $H_2O$ (△), RAW OP (□), and GP $H_2O$ (○) in aqueous solutions and $t = 25$ °C. The experimental data were processed using the Langmuir (solid line) and Freundlich (dotted line) models.

highest values of $K_L$, indicating a greater affinity of the material for the REEs. The use of this waste biomass could enhance the marketability of the recovery process, as it is an inexpensive, biodegradable, and widely available material. These are significant advantages for adsorption compared to other extraction techniques used for the recovery/removal of metals from aqueous solutions (*e.g.*, solid–liquid extraction, flotation, coagulation, flocculation, solvent extraction, ion exchange, co-precipitation), which typically involve hazardous chemical reagents [18].

The mean equilibrium pH values of isotherm experimental points ($pH_e$) are reported in Table 5. In all the investigated systems, the $pH_e$ was lower than $pH_i$ of the REE ions solution as the result of an exchange reaction involving metal cation and proton bound to carboxylate on the pomace surface.

Furthermore, given its higher adsorption capacity, the effect of pH on $Nd^{3+}$ and $Dy^{3+}$ adsorption onto BP $H_2O$ was further investigated carrying out isotherm experiments in aqueous solutions at $t = 25$ °C, $pH_i = 3.0$, 4.0. The scatter plot of experimental data ($q_e$ *vs.* $C_e$), together with lines representing Langmuir and Freudlich isotherm model equation are given in Fig. 7. Refined parameters ($q_m$ and $K_L$) together with fitting quality parameters ($R^2$ and RMSE) of the Langmuir and Freundlich models are summarized in Table 5 and Table S6, respectively. Consistently, the Langmuir model provided the best description of the experimental data, as evidenced by the highest $R^2$ and lowest RMSE values. Furthermore, the $q_m$ values obtained for each metal ion at the different pH levels confirmed the single batch experiment findings (see section 3.1), showing a reduction in maximum adsorption capacity of ~37 % for $Nd^{3+}$ and ~60 % for $Dy^{3+}$ comparing the $q_m$ values at $pH_i = 3.0$ and 5.0. In all cases, the sorption capacity of the material towards metal cations increased with pH. As the active site of the material (log $K^H \approx 3.5$) is increasingly deprotonated (≈25 % at pH = 3, ≈75 % at pH = 4, and ≈95 % at pH = 5), then metal binding is favored when the sites are in deprotonated (anionic) form. As regards $Nd^{3+}$ and $Dy^{3+}$, their chemical speciation is quite similar. In the experimental conditions given, below pH = 5, cation hydrolysis is negligible, and they are present as hydrated cations.

The adsorption capacity of the most effective material was further examined by assessing the influence of an ionic medium on the adsorption of $Dy^{3+}$ and $Nd^{3+}$. To this purpose, batch adsorption isotherm experiments were carried out in 0.10 mol/dm$^3$ $NaNO_3$ solutions at $pH_i = 5.0$ and $t = 25$ °C. The experimental data were well described by the Langmuir model (Figs. S10 and S11 of the Supporting Materials). A comparison between $q_m$ calculated in the presence of sodium nitrate and that obtained without background salt revealed a significant decline in adsorption ability. This reduction could be attributed to the shielding effect exerted by the ions resulting from $NaNO_3$ dissociation, as well as the competitive adsorption of $Na^+$ ions, which are present at a concentration of five orders of magnitude higher than that of the cations. Furthermore, the potential formation of ion pairs between nitrate anions and trivalent REE cations should be considered [70], as this interaction may partially neutralize the positive charge of the metal ions, thereby reducing their affinity for the adsorbent.

The adsorption ability of BP $H_2O$ was also evaluated towards $La^{3+}$ ions carrying out other adsorption isotherm experiments at $t = 25$ °C, $pH_i = 5.0$, at low ionic strength and in 0.10 mol/dm$^3$ $NaNO_3$ solution, to evaluate its adsorption ability towards another light REE ion (analogously to $Nd^{3+}$) in the presence and absence of an ionic medium. Once again, in both conditions, Langmuir model well described the collected data (Fig. S11).

By comparing the Langmuir parameters obtained for $La^{3+}$ with those for $Nd^{3+}$ and $Dy^{3+}$ (this latter a heavy REE) collected in Table 5, a comprehensive understanding of the adsorption of REEs ions onto BP $H_2O$ has been achieved. The maximum adsorption capacity values without ionic medium addition were observed towards $Dy^{3+}$, followed by $Nd^{3+}$ and $La^{3+}$, respectively, while the Langmuir constant values

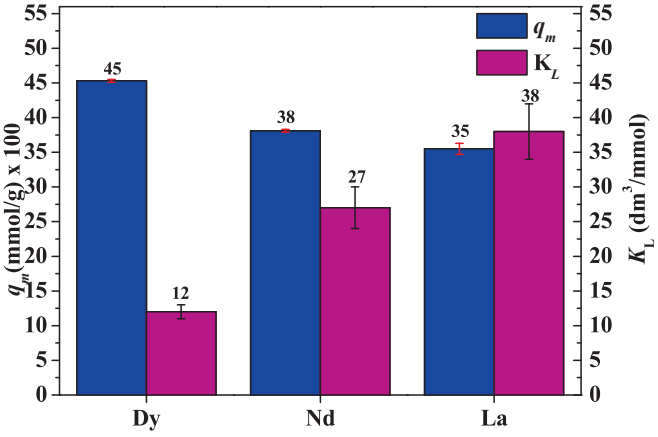


**Fig. 8.** $q_m$ and $K_L$ values of REEs adsorption onto BP $H_2O$ at $pH_i = 5.0$, without ionic medium and $t = 25$ °C.

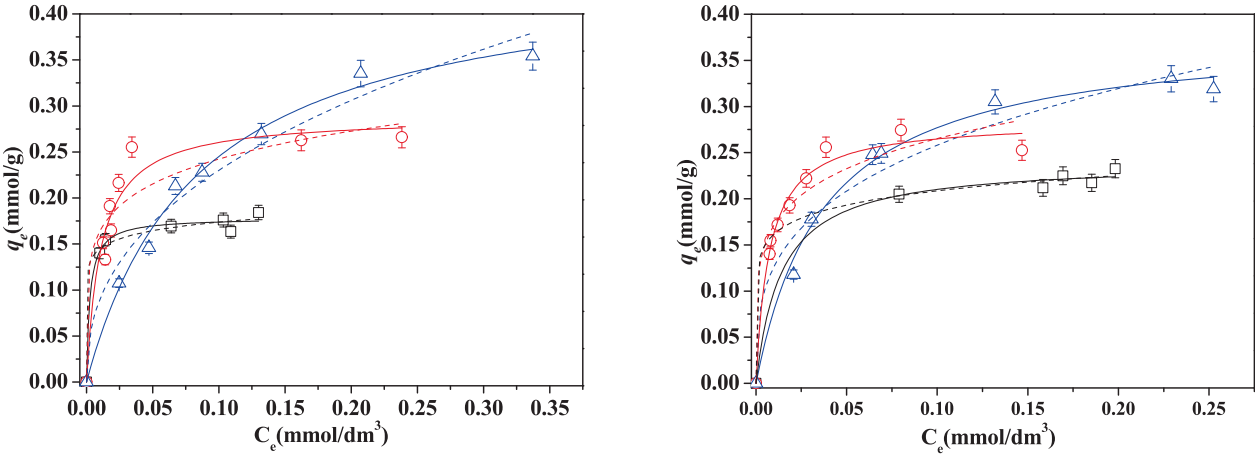


**Fig. 7.** Adsorption isotherms of $Dy^{3+}$ (a) and $Nd^{3+}$ (b) onto BP $H_2O$ in aqueous solutions, at t = 25 °C, at $pH_i = 5.0$ (△), 4.0 (○) and 3.0 (□). The experimental data were processed using the Langmuir (solid line) and Freundlich (dotted line) models.

exhibited an opposite trend (Fig. 8).

Despite their common trivalent charge and similar coordination chemistry, REEs display adsorption behaviors strongly influenced by subtle differences in ionic radius, hydration energy, and coordination geometry. The observed $q_m$ and $K_L$ trends likely reflect variations in hydration shell structure: $La^{3+}$ (1.045 Å) > $Nd^{3+}$ (0.983 Å) > $Dy^{3+}$ (0.912 Å) [70,76]. Larger ions, such as $La^{3+}$, possess more diffuse hydration shells with lower desolvation energies, enabling direct coordination with carboxylates on BP and higher $K_L$ values. Conversely, smaller ions like $Dy^{3+}$ form compact, strongly bound hydration shells that enhance electrostatic interactions with carboxylate and hydroxyl groups, producing denser adsorption layers (higher $q_m$) but incurring greater desolvation penalties. Similar size–hydration effects, favoring heavy REEs, have been reported for lignocellulosic biosorbents such as banana peel–derived adsorbents [19]. The role of the hydration shell on the adsorption of REE ions onto water-treated bergamot pomace is further supported by analyzing the $q_m$ values obtained in the presence of sodium nitrate (Table 5). The introduction of $Na^+$ ions lead to a general decrease in the adsorption capacity due to above-mentioned competitive adsorption processes. However, $La^{3+}$ exhibited the highest $q_m$ values, indicating that its lower solvation energy enables more effective interaction with BP $H_2O$ sites despite the presence of sodium ions.

In order to evaluate the results obtained in this paper for BP $H_2O$ within the framework of waste biomass used for the same purpose of recovering REEs, a comparative analysis of adsorption capacities ($q_m$) is provided in Table 6, including also data for $Ce^{3+}$, $Eu^{3+}$, $Pr^{3+}$, $Sm^{3+}$, and $Tb^{3+}$, which were not considered in this work. To make comparisons among different metal cations, which are featured by different atomic weights, the $q_m$ values were reported, both for experimental and literature data, in mmol/g instead of mg/g. The table is organized grouping results metal by metal and values are ordered from the highest to the lowest and also contains information of which equation was used for the modelling of the kinetic and isotherm experiments.

The sorption performance of BP $H_2O$ lies within the typical range reported for lignocellulosic materials. As far as $La^{3+}$ cation is considered, BP $H_2O$ exhibited a maximum adsorption capacity of 0.35 ± 0.01 mmol/g, lower than that of grapefruit peel (1.24 mmol/g [62]) and orange peel (1.13 mmol/g [28]), but higher than grape stalk (0.26 mmol/g [11]). For $Nd^{3+}$, BP $H_2O$ reached 0.38 ± 0.01 mmol/g, surpassing banana peel (0.33 mmol/g [19]) and bone powder (0.08 mmol/g, [67]) although still lower than banana waste (0.72 mmol/g [19]). The best adsorption result was recorded for $Dy^{3+}$, with 0.45 ± 0.02 mmol/g, outperforming banana peel (0.36 mmol/g [19]), but lower than banana waste (0.81 mmol/g, [19]). A general evaluation of these results indicated that the diversity of performance depends on the sorbent nature. For example, prawn carapace, which is a chitin-based material, resulted very efficient for the recovery of $Ce^{3+}$ (7.13 mmol/g [75]), activated biochar (at pH = 6.5) from cactus fibers, which is a material obtained through a thermal treatment of waste biomass, was capable to recovery $Sm^{3+}$ (2.33 mmol/g [73]). Considering all the differences among the possible waste biomass, the sorption capacities achieved by BP $H_2O$ towards $La^{3+}$, $Nd^{3+}$ and $Dy^{3+}$ fall within an average value.

**Table 6**
Literature data reported for the adsorption of rare earths by different biomasses.

| Adsorbent | REEs | Isotherm model | Kinetic model | $q_m$ (mmol/g) | Ref. |
|---|---|---|---|---|---|
| Prawn carapace | $Ce^{3+}$ | L | N/A | 7.13 | [75] |
| Corn style | $Ce^{3+}$ | L | N/A | 1.78 | [75] |
| Fish scales | $Ce^{3+}$ | L | N/A | 1.43 | [75] |
| Neem sawdust | $Ce^{3+}$ | L | N/A | 1.43 | [75] |
| Eggshell | $Ce^{3+}$ | L | N/A | 1.19 | [75] |
| Orange peel | $Ce^{3+}$ | L | PSO | 1.16 | [28] |
| Grapefruit peel | $Ce^{3+}$ | L | PSO | 1.14 | [62] |
| Pineapple crown | $Ce^{3+}$ | L | N/A | 1.02 | [75] |
| Crab shell | $Ce^{3+}$ | L | N/A | 0.65 | [75] |
| Orange peel | $Ce^{3+}$ | L | N/A | 0.51 | [75] |
| Grape stalk | $Ce^{3+}$ | L | PSO | 0.27 | [11] |
| Banana waste | $Dy^{3+}$ | L | PSO | 0.81 | [19] |
| BP $H_2O$ | $Dy^{3+}$ | L | PSO | 0.45 | This work |
| Banana peel | $Dy^{3+}$ | L | PSO | 0.36 | [19] |
| Bone powder | $Eu^{3+}$ | L | N/A | 1.33 | [67] |
| Crab shell | $Eu^{3+}$ | L | PSO | 0.65 | [68] |
| Banana waste | $Eu^{3+}$ | L | PSO | 0.56 | [19] |
| Banana peel | $Eu^{3+}$ | L | PSO | 0.12 | [19] |
| Modified cactus fibers ($MnO_2$-coated) | $Eu^{3+}$ | L | PFO | 0.08 | [74] |
| Modified cactus fibers | $Eu^{3+}$ | L | PFO | 0.02 | [74] |
| Raw cactus fiber | $Eu^{3+}$ | L | PFO | 0.01 | [74] |
| Prawn carapace | $La^{3+}$ | F | N/A | 1.44 | [69] |
| Grapefruit peel | $La^{3+}$ | L | PSO | 1.24 | [62] |
| Orange peel | $La^{3+}$ | L | PSO | 1.13 | [28] |
| Eggshell | $La^{3+}$ | F | N/A | 0.72 | [69] |
| Pineapple crown | $La^{3+}$ | F | N/A | 0.72 | [69] |
| Crab shell | $La^{3+}$ | F | N/A | 0.65 | [69] |
| Corn style | $La^{3+}$ | F | N/A | 0.55 | [69] |
| BP $H_2O$ | $La^{3+}$ | L | PSO | 0.35 | This work |
| Grape stalk | $La^{3+}$ | L | PSO | 0.26 | [11] |
| Banana waste | $Nd^{3+}$ | L | PSO | 0.72 | [19] |
| BP $H_2O$ | $Nd^{3+}$ | L | PSO | 0.38 | This work |
| Banana peel | $Nd^{3+}$ | L | PSO | 0.33 | [19] |
| Bone powder | $Nd^{3+}$ | L | N/A | 0.08 | [67] |
| Crab shell | $Pr^{3+}$ | L | PFO | 0.48 | [66] |
| Orange peel | $Pr^{3+}$ | L | PSO | 0.42 | [66] |
| Activated biochars from cactus fibers (pH = 6.5) | $Sm^{3+}$ | L | PFO | 2.33 | [73] |
| Activated biochars from cactus fibers (pH = 3.0) | $Sm^{3+}$ | L | PFO | 0.60 | [73] |
| Banana peel | $Tb^{3+}$ | L | PSO | 0.14 | [19] |

L: Langmuir; F: Freundlich; PSO: Pseudo-second-order kinetic model; PFO: Pseudo-first-order kinetic model.

*Adsorption processes thermodynamic parameters*

ITC is a highly sensitive and accurate technique allowing a direct quantification of the heat exchanged during a chemical process. Although it is widely employed for the investigation of chemical solution equilibria (see, e.g., [77–79]), to the best of the authors knowledge no papers have been published yet using the mentioned technique to obtain thermodynamic parameters of interaction between a solid sorbent and metal cations. Adsorption enthalpy change ($\Delta_{sor}H$) is usually indirectly calculated by means of the Van't Hoff equation, considering the temperature dependence of the Langmuir constant, as observable in the case of studies reported on Yb(III), La(III), Ce(III), Sm(III) and Nd(III) adsorption onto Spirulina biomass [27], orange peel [28], activated carbon derived from soybean pods [25], biochar fibers from *Opuntia Ficus Indica* [26], chitosan–polyethylene glycol-polyvinyl alcohol hybrid membrane [80]. However, some authors have highlighted significant discrepancies between the values obtained via Van't Hoff analysis and those directly measured by ITC, due to the inherent limitations and assumptions of the indirect approach [61]. On the contrary, the mentioned analytical technique allows the determination of more robust and independent thermodynamic parameters, as demonstrated by Batista *et al.* [29], who investigated the adsorption of methylene blue by tangerine peel pre-treated with a 0.10 mol/dm$^3$ sodium hydroxide solution.

The $Nd^{3+}$ and $Dy^{3+}$ adsorption enthalpy change ($\Delta_{sor}H$) onto BP $H_2O$ was determined by ITC and the experimental data elaborated using Eq. (14). In addition, Eqs. (15) and (16) were employed for the calculation of the corresponding free Gibbs energy ($\Delta_{sor}G$) and entropy ($\Delta_{sor}S$) change values associated to the sorption process. The results, reported in Table 7 together with literature values on similar systems obtained by the Van't Hoff equation, suggest that the REEs adsorption is a spontaneous ($\Delta_{sor}G < 0$ kJ/mol) and endothermic process ($\Delta_{sor}H > 0$ kJ/mol),

**Table 7**
Literature data reported for thermodynamic parameters for the adsorption of rare earths by different biomasses and methodologies (ITC or Van't Hoff) used.

| Metal Ion | Adsorbent | $\Delta H^0$ (kJ/mol) | $\Delta G^0$ (kJ/mol) | $\Delta S^0$ (J/(mol·K)) | Method | Ref. |
|---|---|---|---|---|---|---|
| $Nd^{3+}$ | BP $H_2O$ | 35 ± 8 [a] | −48 ± 17 [a] | 278 ± 63 [a] | ITC | T. W. [b] |
| $Dy^{3+}$ | BP $H_2O$ | 65 ± 16 | −46 ± 6 | 371 ± 58 | ITC | T. W. [b] |
| $La^{3+}$ | Tangerine Peel | 28.57 | −23.29 | 170.85 | Van't Hoff | [28] |
| $Ce^{3+}$ | Tangerine Peel | 38.34 | −24.13 | 206.18 | Van't Hoff | [28] |
| $Eu^{3+}$ | Cactus Fibers | 39.7 | −31.1 | 237 | Van't Hoff | [26] |
| $Eu^{3+}$ | Phosphorylated Cactus Fibers | 80.9 | −38.2 | 397 | Van't Hoff | [26] |
| $Eu^{3+}$ | MnO2-coated Cactus Fibers | 73.6 | −29.5 | 342 | Van't Hoff | [26] |
| $Yb^{3+}$ | Dried Spirulina Powder | 0.41 | −3.09 | 11.72 | Van't Hoff | [27] |
| $Ce^{3+}$ | Zeolite ZSM-5 | 98.2 | −31.68 | −223.1 | Van't Hoff | [25] |
| $La^{3+}$ | Zeolite ZSM-5 | 73.3 | −27.49 | −155.5 | Van't Hoff | [25] |
| $Nd^{3+}$ | Zeolite ZSM-5 | 96.8 | −33.72 | −211.6 | Van't Hoff | [25] |

[a] ± std. dev.
[b] This work.

indicating that the sorption would be favoured with a temperature increase. The ITC-derived enthalpy changes for $Nd^{3+}$ (+35 ± 8 kJ/mol) and $Dy^{3+}$ (+65 ± 16 kJ/mol) fall above the range typically associated with physisorption ($\Delta H = -5$ to $-20$ kJ/mol) and approach values reported for chemisorption (−40 to −120 kJ/mol) as noted in general adsorption reviews [81,82]. The values obtained for the sorption of REE cations onto BP in this work, exhibiting positive $\Delta_{sor}H$ (+35 and + 65 kJ/mol, for Nd(III) and Dy(III), respectively) and high $\Delta_{sor}S$ values (+278 and + 371 J/(mol·K), same order) suggest entropy-driven mechanisms involving inner-sphere surface complexation and partial dehydration of REE aquo-complexes. In fact, Choppin [83–86] reports that when inner sphere complexes of 4f cations are formed, the primary hydration sphere is sufficiently disrupted that its contribution exceeds that of the cation–ligand interaction, resulting in an endothermic enthalpy change and a positive entropy change. Moreover, the greater enthalpy change value obtained for $Dy^{3+}$ compared to $Nd^{3+}$ reflects the lanthanide contraction, which results in a lower ionic radius and a more compact and strongly bound hydration sphere, as also above suggested when discussing data on Langmuir constants (Fig. 8). The release of water molecules from the hydration sphere into the bulk increases the number of accessible microstates, resulting in a significant entropic increase, which balances the positive enthalpy change values and makes the process spontaneous ($\Delta_{sor}G < 0$). This suggests a specific and direct adsorption on the oxygenated sites of the biomass, in agreement with the hard behaviour of lanthanides, according to Pearson [87]. The results reported by Batista [29] showed that the process was exothermic ($\Delta_{sor}H \sim -20$ to $-25$ kJ/mol) and entropy-driven by the release of solvation water from hydrophobic domains, resulting in a modest $\Delta_{sor}S$ (~35 J/(mol·K)). In contrast, the adsorption of $Nd^{3+}$ and $Dy^{3+}$ onto bergamot pomace required a significantly higher energy input for dehydration ($\Delta_{sor}H > 30$ kJ/mol) accompanied by much higher entropy gain ($\Delta_{sor}S >$ 270 J/(mol·K)), which reflects the breakdown of structured hydration shells and the formation of inner-sphere surface complexes. These differences underscore the strong dependence of thermodynamic behaviour on the chemical nature of the adsorbate and confirm the distinct adsorption pathways involved in metal–biosorbent versus dye-biosorbent systems.

To better contextualize our findings, in Table 7 our ITC results are compared with van't Hoff-derived data from literature for the sorption on REE cations onto biosorbents.

REE adsorption process is always endothermic, even though enthalpy changes vary considerably depending on the biosorbent. Our results ($\Delta H = +35$ to +65 kJ/mol) are comparable or higher than values obtained for lanthanide sorption on tangerine peel (28–38 kJ/mol), cactus fibers (39–80 kJ/mol), and much lower than those for Zeolite ZSM-5 (up to 98 kJ/mol), suggesting that the pomace materials interact with REEs *via* relatively strong, selective, and energetically demanding processes, most likely involving coordination to carboxylate and hydroxyl groups after partial disruption of the hydration shell.

As far as entropy change values are concerned, most of the values are largely positive, except for what found in the case of Zeolite ZSM-5 that were found to be negative.

The $\Delta_{sor}G$ values could also provide insight into the adsorption mechanism: according to thermodynamic criteria [88], since the data obtained using BP $H_2O$ range between −48 to −46 kJ/mol, the $Nd^{3+}$ and $Dy^{3+}$ adsorption processes could potentially occur by means of a combination of physical and chemical-type electrostatic interactions.

These results suggest that the REE–biomass interactions in this case involve a combination of electrostatic attraction and weak coordination to functional groups, consistent with the absence of major spectral shifts in FT-IR [81,82]. It should be emphasized that $\Delta H$ alone is not sufficient to classify the adsorption mechanism. In this study, the endothermic nature of the process, combined with high $\Delta_{sot}S$ values, lack of strong FT-IR band shifts, and fast PSO-type kinetics, suggests that the mechanism involves entropy-driven, non-covalent interactions likely comprising electrostatic attraction and weak coordination rather than true chemisorption.

*Reuse and recovery*

The cost and environmental footprint of REEs recovery can be significantly minimized by regenerating and reusing adsorbent materials. To investigate this aspect, a series of four adsorption/desorption cycles was carried out. A 0.1002 mol/dm$^3$ $HNO_3$ solution was employed as the desorbing agent. The adsorption capacity in each cycle was calculated using Eq. (1), while the amount of REE cation desorbed was obtained by Eq. (12); data obtained for the adsorption/desorption steps are reported in Fig. S13(a–f). The desorption efficiency for each cycle was determined using Eq. (13). These parameters were used to monitor both the stability of the biosorbent and the effectiveness of REEs recovery over consecutive reuse cycles. As shown in Fig. 9 (9a for $Dy^{3+}$ and 9b for $Nd^{3+}$), BP $H_2O$ exhibited the highest stability in recovery performance across the four cycles. For $Dy^{3+}$, the recovery efficiency decreased only from 98.8 % in the first cycle to 90.2 % in the fourth, while for $Nd^{3+}$ it lowered from 97.0 % to 88.9 %. This corresponds to an overall loss of less than 9 %, demonstrating the strong potential of the material for multiple use without the need for pre-treatment. In contrast, GP $H_2O$ showed a more pronounced decrease ($Dy^{3+}$: from 92.2 % to 52.0 %; $Nd^{3+}$: from 96.2 % to 35.3 %), while RAW OP suffered the steepest decline ($Dy^{3+}$: from 91.4 % to 45.0 %; $Nd^{3+}$: from 95.3 % to 24.8 %). Nevertheless, the desorption with nitric acid ensured the complete recovery of the adsorbed metals at each step. These findings confirm BP $H_2O$ as a sustainable and durable biosorbent for the repeated recovery of $Nd^{3+}$ and $Dy^{3+}$ from aqueous solutions.

In literature, Lapo and colleagues [19] checked one cycle of $Nd^{3+}$, $Dy^{3+}$, $Eu^{3+}$ and $Tb^{3+}$ desorption by banana waste biomass using 0.01 mol/dm$^3$ EDTA and 0.10 mol/dm$^3$ HCl solutions as desorbing agents. The author obtained a desorption efficiency of 97 % and 40 % by testing the chelating agent and the inorganic acid, respectively. Varshini *et al.* [69] evaluated the reusability of orange peel for the $Pr^{3+}$ adsorption/desorption employing a 0.10 mol/dm$^3$ NaOH solution for the metal elution, observing that the biomass could be efficiently reused for 7 cycles, with a desorption efficiency of 94 – 95 % for each of them. Birungi and Chirwa [71] used freshwater algal biomasses for La(III)

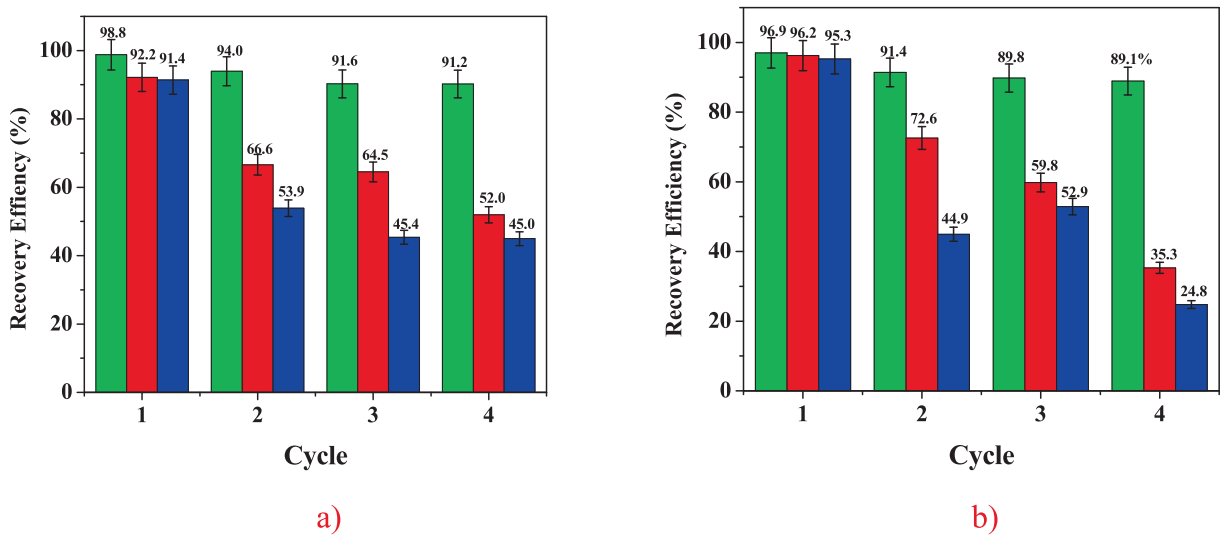


**Fig. 9.** Recovery efficiencies (RE%) of (a) $Dy^{3+}$ and (b) $Nd^{3+}$ over four consecutive adsorption/desorption cycles using BP $H_2O$ (green), GP $H_2O$ (red), and RAW OP (blue) as biosorbents. (For interpretation of the references to colour in this figure legend, the reader is referred to the web version of this article.)

adsorption and checked the metal recovery with a 0.10 mol/$dm^3$ $HNO_3$ solution in three elution cycles, finding that the *Desmodesmus multivariabilis* was the most efficient with a recovery of ~99.6 %. Hussien [73] carried out three cycles of $La^{3+}$ desorption experiments in the presence of *Pleurotus ostreatus* biosorbent and dilute hydrochloric and nitric acid solutions ($C_{H+}$ = 0.10, 0.20, 0.30 mol/$dm^3$), determining that

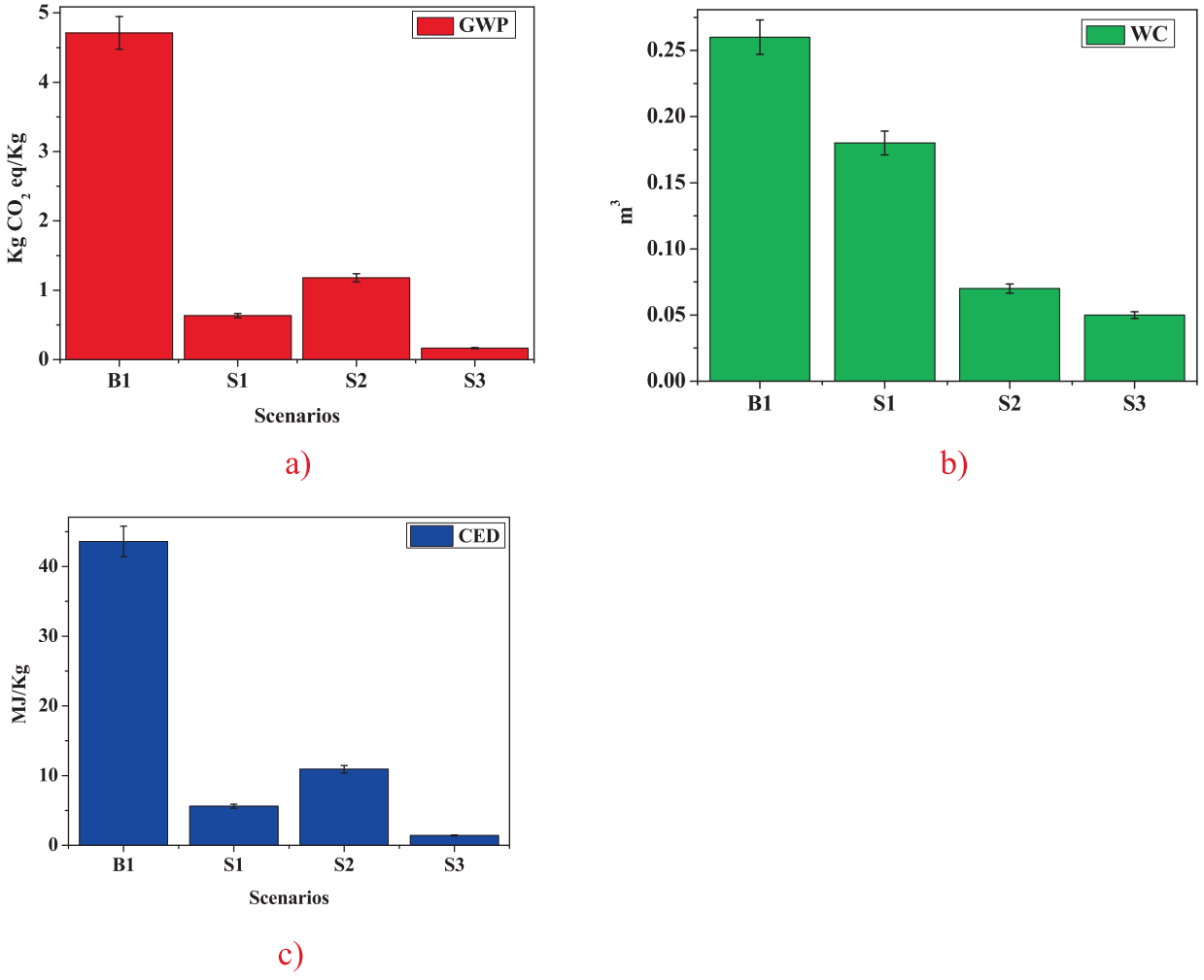


**Fig. 10.** Bar plot of Global Warming (a), Water Consumption (b) and Cumulative Energy Demand (c) for the production of 1 kg of biosorbent under all the four scenarios.

0.10 mol/dm$^3$ $HNO_3$ solution was the most suitable, with elution efficacies between 67 % and 97 %.

*Environmental and economic evaluation*

In recent years, the development and application of alternative sorbents derived from industrial and agricultural by-products, such as biochar and activated carbon, have gained global interest. Several LCA studies have evaluated the environmental impacts of biochar production [48,89,90]. These studies highlight that feedstock-type, pyrolysis technology and processing temperature play significant roles in determining overall environmental performance. Moreover, as stated by Alipanah *et al.* [91], REEs adsorption capacity and reusability of biosorbents are critical to their environmental and economic viability. In this context, biosorbents derived from agricultural by-products, particularly those requiring minimal processing energy, offer promising potential for sustainable resource recovery.

As a part of this study, the environmental and economic performance of BP $H_2O$ produced under laboratory-scale conditions was evaluated. Experimental inventory data were analyzed through both LCA and TEA methodologies, providing a dual-perspective assessment of BP $H_2O$ sustainability for REEs recovery. Fig. 10a and b summarize GW, WC and CED scores associated to the production of 1 kg of BP $H_2O$, evaluated across the four scenarios.

The real case (B1) yields the highest environmental impact (GW: 4.22 kg $CO_2$ eq; WC: 0.26 m$^3$; CED: 43.6 MJ), primarily due to inefficient drying process. Scenario S1, which implements an improved drying method, significantly reduced GW, WC and CED to 0.55 kg $CO_2$ eq, 0.18 m$^3$ and 5.6 MJ, respectively. Scenario S2, which involves biosorbent regeneration, offers moderate improvements over the real case, although not as effective as the energy-efficient drying in S1. The optimized scenario (S3), simulating the industrial-scale drying of BP $H_2O$ together with its regeneration, achieves the lowest environmental burdens (GW: 0.14 kg $CO_2$ eq; WC: 0.05 m$^3$; CED: 1.4 MJ). Notably, the trend in GW closely mirrors that of CED, indicating that electricity consumption is the dominant contributor to carbon emissions, while the impacts from water and chemical use remain minimal.

Following the environmental assessment, a TEA was conducted to estimate production costs in €/kg of BP $H_2O$, as shown in Fig. 11.

The real case (B1) shows the highest estimated cost at 13.64 €/kg, whereas the optimized scenario (S3) reduces it significantly to 2.99 €/kg. The acid required for regenerating BP $H_2O$, used in the S2 and S3 scenarios, had minor economic relevance. Notably, water consumption emerged as the most impactful economic factor; its reduction in S2 and S3 proved more cost-effective than solely implementing improved drying (S1). These results highlight the importance of water management, energy efficiency and sorbent reuse in optimizing the cost-performance ratio. When compared to conventional biosorbents, BP $H_2O$ demonstrates competitive performance. Activated carbon typically exhibits GWP values around 6.6 kg $CO_2$ eq/kg and CED above 97 MJ/kg due to its high-temperature processing requirements. In contrast, biochar, owing to its lower energy demand, tends to have a smaller environmental footprint and may even become carbon-negative when applied to soil [48]. From an economic standpoint, the production of BP $H_2O$ demonstrates promising cost performance, particularly when extrapolated to industrial-scale scenarios. In the optimized scenario (S3), production costs fall within or below the range reported in the literature: activated carbon and biochar average 5.6 $/kg and 5 $/kg [89], respectively, with some sources citing values as low as 1.06 $/kg for date palm biochar and 1.34 $/kg for activated carbon [48].

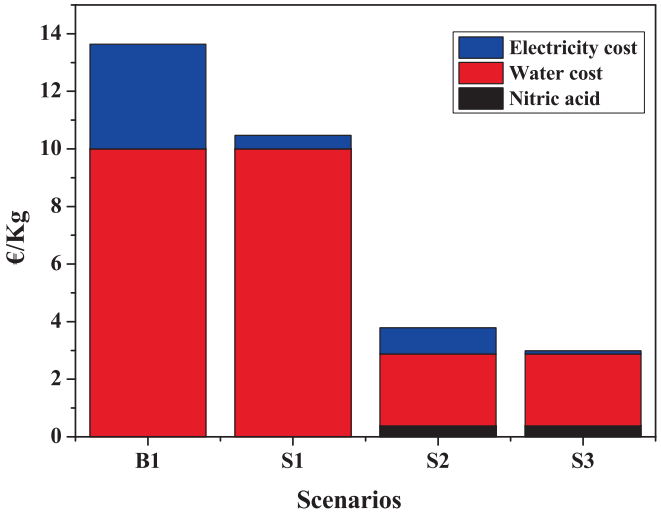


**Fig. 11.** Bar plot of Techno-Economic Assessment (TEA) for the production of 1 kg of biosorbent under all the four scenarios.

From all of the above, the preliminary techno-economic and environmental assessment suggests that BP $H_2O$ is a viable and competitive biosorbent for REEs recovery. Its potential is particularly strong in applications where low-cost agricultural residues and energy-efficient processing strategies can be leveraged to minimize both economic and environmental impacts.

## Conclusions

This study explored the valorization of agri-food industrial waste biomasses, specifically bergamot, grape and olive pomaces, for the recovery of rare earth elements (REEs), such as $Nd^{3+}$, $La^{3+}$ and $Dy^{3+}$ ions, from aqueous solutions. The adsorption performance varied among the tested biomasses, likely influenced by their surface properties and functional groups. The sorption process followed pseudo-second order kinetic, with equilibrium reached in approximately 120 min. The isotherm batch experiments were modeled by means of a Langmuir model equation. Among the tested materials, BP $H_2O$ exhibited the highest adsorption capacity, particularly for $Dy^{3+}$ at $pH_i = 5.0$ in the absence of ionic medium ($q_m = 0.45 \pm 0.02$ mmol/g), followed by $Nd^{3+}$ ($q_m = 0.38 \pm 0.01$ mmol/g) and $La^{3+}$ ($q_m = 0.35 \pm 0.01$ mmol/g). The sorption efficiency decreased upon the addition of ionic medium and the acidification of solutions. The interaction between metal cations and biosorbent was confirmed by SEM-EDX and ATR FT-IR spectroscopies. The former technique allowed the investigation of morphology variation induced by contact with REEs cations and ascertained the presence of both $Nd^{3+}$ and $Dy^{3+}$ on the pomace surface. The latter revealed a new band at ~420 cm$^{-1}$ in the spectra of BP $H_2O$ samples after sorption with $Nd^{3+}$ and $Dy^{3+}$, absent in the starting samples, attributed to the interaction between the metal cations and O-donor groups on the pomace surface. Adsorption isotherm modeling using Langmuir equation showed excellent fits with the experimental data, suggesting the homogeneous distribution of surface adsorption sites. Thermodynamic parameters of interaction between sorbent and REEs cations were directly determined by ITC providing, for the first time and addressing a critical knowledge gap in the field, a more robust and accurate alternative to the traditional Van't Hoff approach. The results suggested that REE cation sorption processes are spontaneous, endothermic and entropic in nature. The adsorption process investigated here showed a better fit with the PSO model, which is often associated with systems where chemisorption or complexation phenomena are involved. Nevertheless, the thermodynamic analysis performed via ITC revealed positive enthalpy changes ($\Delta_{sor}H = +35 \pm 8$ kJ/mol for $Nd^{3+}$ and $+65 \pm 16$ kJ/mol for $Dy^{3+}$), indicating an endothermic process. This, together with high positive entropy values and the absence of major FT-IR spectral shifts, suggests an entropy-driven adsorption mechanism, likely involving a combination of electrostatic interactions, weak surface complexation, and partial desolvation of REE ions upon interaction with surface sites of BP.

Besides converting waste material into a valuable resource, in view of the possible scaling up of the process, the reusability of the sorbent material through multiple adsorption/desorption cycles was verified to enhance the overall sustainability of the process. Desorption experiments demonstrated successful biomass regeneration across four adsorption/desorption cycles, with a negligible performance contraction (~9 %). This is very significant since when planning an integrated protocol for the continuous recovery of valuable materials, both $q_m$ values and reusability features must be taken into account. A combined environmental (LCA) and economic (TCA) assessment of the BP $H_2O$ production revealed that, while lab-scale impacts are significant, scalability may lead to substantial improvements. In the optimized scenario (S3), GWP and CED were reduced by over 85 %, while production costs dropped below 2.99 €/kg. Further research is required to validate these findings on a pilot scale and to assess performance in real matrices.

These findings, integrated with desorption and reuse analysis and comprehensive environmental and techno-economic evaluations, provide a holistic perspective on the feasibility and sustainability of this approach, contributing valuable insights into eco-efficient strategies for the recovery of CRMs, such as $Nd^{3+}$, $La^{3+}$ and $Dy^{3+}$, ranking bergamot pomace as a promising sustainable resource.

## CRediT authorship contribution statement

**Salvatore Giovanni Michele Raccuia:** Writing – original draft, Resources, Methodology, Investigation, Formal analysis. **Emanuele Zanda:** Writing – original draft, Validation, Methodology, Formal analysis, Data curation. **Clemente Bretti:** Validation, Resources, Methodology, Formal analysis, Data curation. **Mauro Formica:** Writing – original draft, Visualization, Methodology, Formal analysis, Data curation. **Eleonora Macedi:** Writing – original draft, Methodology, Investigation, Formal analysis, Data curation. **Andrea Melchior:** Writing – original draft, Resources, Methodology, Formal analysis, Data curation. **Marilena Tolazzi:** Writing – original draft, Validation, Methodology, Formal analysis, Data curation. **Alberto Pettignano:** Writing – original draft, Validation, Methodology, Formal analysis, Data curation. **Nicola Muratore:** Validation, Software, Resources, Investigation, Formal analysis. **Davide Lascari:** Software, Investigation, Formal analysis, Data curation. **Edoardo Teresi:** Methodology, Investigation, Formal analysis, Data curation. **Cristian Chiavetta:** Writing – original draft, Methodology, Investigation, Data curation. **Giovanna De Luca:** Writing – original draft, Visualization, Resources, Methodology, Conceptualization. **Anna Irto:** Writing – original draft, Validation, Methodology, Formal analysis, Data curation, Conceptualization. **Concetta De Stefano:** Visualization, Validation, Software, Resources, Conceptualization. **Paola Cardiano:** Writing – review & editing, Writing – original draft, Visualization, Supervision, Funding acquisition, Conceptualization. **Gabriele Lando:** Writing – review & editing, Writing – original draft, Visualization, Supervision, Project administration, Methodology, Funding acquisition, Conceptualization.

## Funding

This work was supported by Next Generation EU, Missione 4, Componente 1, CUP J53D23007540006—PRIN_2022HYH95P.

## Declaration of competing interest

The authors declare that they have no known competing financial interests or personal relationships that could have appeared to influence the work reported in this paper.

## Appendix A. Supplementary data

Supplementary data to this article can be found online at https://doi.org/10.1016/j.jiec.2025.09.008.

## Data availability

Data will be made available on request.

## References

[1] P. Chen, E. Ilton, Z. Wang, K. Rosso, X. Zhang, Appl. Geochem. 175 (2024) 106158.
[2] S.-L. Liu, H.-R. Fan, X. Liu, J. Meng, A.R. Butcher, L. Yann, K.-F. Yang, X.-C. Li, Ore Geology Rev. 157 (2023) 105428.
[3] M. Koese, S. van Nielen, J. Bradley, R. Kleijn, Appl. Energy 388 (2025) 125707.
[4] U.S.G. Survey (Ed.), Rare Earths, Mineral Commodity Summaries, 2014, pp. 128–129.
[5] Adamas Intelligence Statista (Ed.), NRCan, Roskill, 2023.
[6] A. Gupta, E. Williams, G. Gaustad, Resour. Conserv. Recycl. 207 (2024) 107612.
[7] European Commission, https://commission.europa.eu/strategy-and-policy/priorities-2019-2024/european-green-deal_it (2024).
[8] Y. Bian, S. Guo, Y. Xu, K. Tang, W. Ding, Rare Met. 34 (2015).
[9] S. Cheng, W. Li, Y. Han, Y. Sun, P. Gao, X. Zhang, J. Rare Earths 42 (2024) 629–642.
[10] T. Prados, T. Cruz Tabosa Barroso, T. Forster-Carneiro, G. Lovon-Canchumani, L. Colpini, Clean Technol. Environ. Policy (2024) 1–24.
[11] R.N.F. da Silva, P. de Azevedo Mello, A. Penteado Holkem, L.F.O. Silva, M.L. S. Oliveira, A. Nawaz, S. Manoharadas, G.L. Dotto, Environ. Sci. Pollut. Res. Int. 30 (2023) 118366–118376.
[12] İ. Çelik, D. Kara, C. Karadaş, A. Fisher, S.J. Hill, Talanta 134 (2015) 476–481.
[13] S. Chen, X. Cheng, Y. He, S. Zhu, D. Lu, Microchim. Acta 180 (2013).
[14] L. Stoy, J. Xu, Y. Kulkarni, C.-H. Huang, ACS Sustain. Chem. Eng. 10 (2022) (1834) 11824.
[15] M. Hermassi, M. Granados, C. Valderrama, C. Ayora, J.L. Cortina, J. Environ. Chem. Eng. 9 (2021) 105906.
[16] M. Moussa, M.M. Ndiaye, T. Pinta, V. Pichon, T. Vercouter, N. Delaunay, Anal. Chim. Acta 963 (2017) 44–52.
[17] A. Mosai, L. Chimuka, E. Cukrowska, I. Kotzé, H. Tutu, Water Air Soil Pollut. 230 (2019).
[18] V. Famobuwa, D. Talan, O. Sanyal, S. Grushecky, H. Amini, J. Rare Earths (2025).
[19] B. Lapo, J.J. Bou, J. Hoyo, M. Carrillo, K. Peña, T. Tzanov, A.M. Sastre, Environ. Pollut. 264 (2020) 114409.
[20] B. Xiao, L. Huang, W. Huang, D. Zhang, X. Zeng, X. Yao, J. Rare Earths 40 (2021).
[21] O. Artiushenko, R. Silva, V. Zaitsev, Sustain. Mater. Technol. 37 (2023) e00681.
[22] S. Babu, S. Singh Rathore, R. Singh, S. Kumar, V.K. Singh, S.K. Yadav, V. Yadav, R. Raj, D. Yadav, K. Shekhawat, O. Ali Wani, Bioresour. Technol. 360 (2022) 127566.
[23] S.G.M. Raccuia, E. Zanda, C. Bretti, M. Formica, E. Macedi, A. Melchior, M. Tolazzi, M. Sanadar, D. Lascari, G. De Luca, A. Irto, C. De Stefano, P. Cardiano, G. Lando, Molecules 29 (2024) 5735.
[24] A. Irto, S.G.M. Raccuia, G. Lando, C. De Stefano, K. Arena, T.M.G. Salerno, A. Pettignano, F. Cacciola, L. Mondello, P. Cardiano, Microchem. J. 193 (2023) 109183.
[25] R.F. Pinheiro, A. Grimm, M.L.S. Oliveira, J. Vieillard, L.F.O. Silva, I.A.S. De Brum, É.C. Lima, M. Naushad, L. Sellaoui, G.L. Dotto, G.S. dos Reis, Chem. Eng. J. 471 (2023) 144484.
[26] M. Prodromou, I. Pashalidis, Desalin. Water Treat. 57 (2016) 5079–5088.
[27] Q. Shu, C.-F. Liao, W.-Q. Zou, B.-Q. Xu, Y.-H. Tan, Trans. Nonferrous Met. Soc. China 31 (2021) 1127–1139.
[28] M. Torab-Mostaedi, Chem. Ind. Chem. Eng. Q. 19 (2013) 79–88.
[29] L.M.S. Batista, J.A.T. Barboza, T.F. Souza, A.B. Mageste, I.A. Marques, L.L.B. S. Nascimento, L.H.M. da Silva, G.M.D. Ferreira, Colloids Surf. A Physicochem. Eng. Asp. 704 (2025) 135423.
[30] S. Schiewer, A. Balaria, Chem. Eng. J. 146 (2009) 211–219.
[31] S. Schiewer, M. Iqbal, J. Hazard. Mater. 177 (2010) 899–907.
[32] U. Suryavanshi, S.R. Shukla, Ind. Eng. Chem. Res. 49 (2010) 11682–11688.
[33] N. Chiron, R. Guilet, E. Deydier, Water Res. 37 (2003) 3079–3086.
[34] Y.S. Ho, G. McKay, Process. Biochem. 34 (1999) 451–465.
[35] S. Lagergren, Handlingar 24 (1898) 1–39.
[36] E.D. Revellame, D.L. Fortela, W. Sharp, R. Hernandez, M.E. Zappi, Clean. Eng. Technol. 1 (2020) 100032.
[37] K.L. Tan, B.H. Hameed, J. Taiwan Inst. Chem. Eng. 74 (2017) 25–48.
[38] K.H. Chu, M. Hashim, G. Hayder, J. Mol. Liq. 409 (2024) 125466.
[39] R. Chandrasekar, P. Prakash, D. Ghosh, S. Narayanasamy, Environm. Res. 260 (2024) 119579.
[40] V.H. Freundlich, Angew. Chem. 14 (1907) 749–750.
[41] I. Langmuir, J. Am. Chem. Soc. 40 (1918) 1361–1403.
[42] H.N. Tran, S.-J. You, A. Hosseini-Bandegharaei, H.-P. Chao, Water Res. 120 (2017) 88–116.
[43] International Organization for Standardization, in: ISO 14040. Environmental Management—Life Cycle Assessment—Principles and Framework, Geneva, Switzerland (2006).
[44] International Organization for Standardization, in: ISO 14044. Environmental Management—Life Cycle Assessment—Requirements and Guidelines, Geneva, Switzerland (2006).
[45] S. Mahlan, O. Tokede, A.M. Sadick, G.P. Costin, Int. J. Life Cycle Assess. 30 (2025) 1623–1650.
[46] B. Raccary, P. Loubet, C. Pérès, G. Sonnemann, Adv. Sample Prep. 1 (2022).

[47] G. Wernet, C. Bauer, B. Steubing, J. Reinhard, E. Moreno-Ruiz, B. Weidema, Int. J. Life Cycle Assess. 21 (2016) 1218–1230.
[48] J. Shaheen, Y.H. Fseha, B. Sizirici, Heliyon 8 (2022) e12388.
[49] G. Landi, M. Benedetti, M. Sforzini, E. Eslami, G. Pataro, Foods 14 (2025) 2239.
[50] Autorità di Regolazione per Energia, Reti e Ambiente, in: Relazione annual, 2024.
[51] Sigma Aldrich, 2025.
[52] F. Piccinno, R. Hischier, S. Seeger, C. Som, J. Clean. Prod. 135 (2016) 1085–1097.
[53] M. Curiel-Fernández, M. Bueno-Herrera, Z. Guadalupe, B. Ayestarán, S. Pérez-Magariño, Molecules 28 (2023) 6770.
[54] I. Gómez Cruz, M.d.M. Contreras, I. Romero, J. Ind. Eng. Chem. 96 (2021).
[55] M. Spinei, M. Oroian, in: The Potential of Grape Pomace Varieties as a Dietary Source of Pectic Substances, 2021.
[56] M. Lucarini, A. Durazzo, J. Kiefer, A. Santini, G. Lombardi-Boccia, E.B. Souto, A. Romani, A. Lampe, S. Ferrari Nicoli, P. Gabrielli, N. Bevilacqua, M. Campo, M. Morassut, F. Cecchini, Foods 9 (2020) 10.
[57] V.-P. Dinh, T.-D.-T. Huynh, H.M. Le, V.-D. Nguyen, V.-A. Dao, N.Q. Hung, L. A. Tuyen, S. Lee, J. Yi, T.D. Nguyen, L.V. Tan, RSC Adv. 9 (2019) 25847–25860.
[58] M. Torab-Mostaedi, M. Asadollahzadeh, A. Hemmati, A. Khosravi, J. Taiwan Inst. Chem. Eng. 44 (2013) 295–302.
[59] F. Pagnanelli, S. Mainelli, F. Veglio, L. Toro, Chem. Eng. Sci. 58 (2003) 4709–4717.
[60] M. Iqbal, S. Schiewer, R. Cameron, J. Chem. Technol. Biotechnol. 84 (2009) 1516–1526.
[61] S.G. Lanas, M. Valiente, E. Aneggi, A. Trovarelli, M. Tolazzi, A. Melchior, RSC Adv. 6 (2016) 42288–42296.
[62] M. Torab-Mostaedi, M. Asadollahzadeh, A. Hemmati, A. Khosravi, Rev. Chem. Intermed. 41 (2015).
[63] N. Yushin, I. Zinicovscaia, L. Cepoi, T. Chiriac, L. Rudi, D. Grozdov, Materials 15 (2022) 6101.
[64] R. Oliveira, P. Hammer, E. Guibal, J.-M. Taulemesse, O. Garcia, Chem. Eng. J. 239 (2014) 381–391.
[65] S. Amiri, H. Shokrollahi, J. Magn. Magn. Mater. 345 (2013) 18–23.
[66] S. Anselmo, T. Avola, K. Kalouta, S. Cataldo, G. Sancataldo, N. Muratore, V. Foderà, V. Vetri, A. Pettignano, Int. J. Biol. Macromol. 239 (2023) 124276.
[67] E.I. Cadogan, C.-H. Lee, S.R. Popuri, H.-Y. Lin, Int. Biodeterior. Biodegrad. 95 (2014) 232–240.
[68] L. Hadjittofi, S. Charalambous, I. Pashalidis, J. Rare Earths 34 (2016) 99–104.
[69] C.J. Varshini, D. Pramanik, N. Das, Ecol. Eng. 81 (2015) 321–327.
[70] N. Muratore, D. Lascari, S. Cataldo, S.G.M. Raccuia, G. Lando, P. Lo Meo, V. Chiodo, S. Maisano, F. Urbani, A. Pettignano, J. Rare Earths (2024).
[71] Z. Birungi, E. Chirwa, Bioresour. Technol. 160 (2014).
[72] M. Butnariu, P. Negrea, L. Lupa, M. Ciopec, A. Negrea, M. Pentea, I. Sarac, I. Samfira, Int. J. Environ. Res. Public Health 12 (2015) 11278–11287.
[73] S. Hussien, Int. J. Biomed. Res. 2 (2014) 26–036.
[74] C. Varshini, N. Das, Res. J. Pharm., Biol. Chem. Sci. 5 (2014) 402–408.
[75] C. Varshini, N. Das, Res. J. Pharm. Biol. Chem. Sci. 5 (2014) 88–94.
[76] R.D. Shannon, Acta Crystallogr. A 32 (1976) 751–767.
[77] C. Bretti, C. De Stefano, P. Cardiano, S. Cataldo, A. Pettignano, G. Arena, C. Sgarlata, G. Ida Grasso, G. Lando, S. Sammartano, J. Mol. Liq. 343 (2021) 117699.
[78] C. Sgarlata, V. Zito, G. Arena, Anal. Bioanal. Chem. 405 (2013) 1085–1094.
[79] C. Bretti, C. De Stefano, G. Lando, K. Majlesi, S. Sammartano, J. Sol. Chem. 46 (2017) 1903–1927.
[80] C. Bulin, R. Zheng, T. Guo, Int. J. Biol. Macromol. 282 (2024) 136845.
[81] G.L. Dotto, G. McKay, J. Environ. Chem. Eng. 8 (2020) 103988.
[82] K.Y. Foo, B.H. Hameed, Chem. Eng. J. 156 (2010) 2–10.
[83] G.R. Choppin, J. All. Compd. 249 (1997) 1–8.
[84] G.R. Choppin, J. All. Compd. 249 (1997) 9–13.
[85] G.R. Choppin, Radiochim. Acta 32 (1983) 43–54.
[86] G.R. Choppin, Pure Appl. Chem. 27 (1971) 23–42.
[87] R.G. Pearson, J. Chem. Educ. 45 (581) (1968) 643.
[88] P.W. Atkins, J. De Paula, Phys. Chem. Macmillan High. Educ. (2002).
[89] H.A. Alhashimi, C.B. Aktas, Resour. Conserv. Recycl. 118 (2017) 13–26.
[90] S.S. Harsono, P. Grundman, L.H. Lau, A. Hansen, M.A.M. Salleh, A. Meyer-Aurich, A. Idris, T.I.M. Ghazi, Resour. Conserv. Recycl. 77 (2013) 108–115.
[91] M. Alipanah, D.M. Park, A. Middleton, Z. Dong, H. Hsu-Kim, Y. Jiao, H. Jin, ACS Sustain. Chem. Eng. 8 (2020) 17914–17922.